Technical University of Munich
Max Planck Institute for Extraterrestrial Physics
High-Energy Astrophysics

Bachelor's Thesis in Physics

Gamma-ray signatures of time variable astrophysical sources observed with INTEGRAL

Signaturen der Gamma-Strahlung von zeitlich variablen astrophysikalischen Quellen beobachtet mit INTEGRAL

Antonia Drescher

09. April 2018

Supervisor: Prof. Dr. Roland Diehl

Contents

1 Introduction

In astrophysics, most of the time, pictures are taken from celestial objects that evolve over millions or billions of years, for example, the luminosity of our Sun does not change for 10 billion years. But there are also phenomena in our Universe that evolve on much shorter timescales and these objects are called transients.

In some circumstances, these transients emit gamma-rays that are high-energy photons of energies larger than 100 keV and wavelengths of 10^{-12} m. They can be produced in several physical processes such as radioactive decay that occurs in the nucleus of an atom when one element changes to another. Some nuclei are left in an excited state by these changes and de-excite to their ground state by emitting photons of characteristic energies. For the production of radioactive nuclei, extreme physical conditions are required. They can be found in powerful phenomena such as the explosion of massive stars at the end of their stellar evolution, called supernovae or the ejection of accreted matter in a binary system of white dwarfs, called novae. At very high temperatures, radioactive nuclei are synthesized that release energy in form of photons. Gamma-rays can also be produced through the acceleration of charged particles in magnetic fields. This causes the particles to emit photons in the gamma-ray energy range. Another production mechanism is due to the collision of heavy particles with energies MeV to TeV. When cosmic rays strike protons or atomic nuclei, neutral pions are produced that are unstable and decay into two photons [1].

Another source of high-energy photons are gamma-ray bursts (GRB) whose origin is unknown, in general. However, the spectra of these phenomena can be measured. The duration distribution of GRBs is bimodal, which means that there could be two possible mechanisms for the production of GRBs. The emission of gamma-rays from these phenomena can provide information about their 'motors'.

In addition to the measured spectrum, the time variability of scientific objects can provide information about their event duration. In order to do research studies with not only a single object, but with a population of similar objects, they first must be found in the data.

These data of time variable astrophysical sources can be received from the International Gamma Ray Astrophysics Laboratory (INTEGRAL). Its goal is the spectroscopy of photons in the energy range 15 keV to 10 MeV and also the imaging and positioning of energetic phenomena described above [2]. The spectrometer SPI on board the spacecraft is surrounded by an omni-directional veto system, the anticoincidence shield that detects photons with energies above 75 keV. Therefore, it is suitable for finding, describing, and analyzing populations of gamma-ray emitting sources.

The ACS data archive contains count rate data from 15 years now. This means that a retrospective search can be made, for example, for nova outbursts, because gamma-rays from novae arrive earlier at the detectors than optical light. Furthermore, undiscovered GRBs can be found in the ACS light curve. For this, the ACS data must be analyzed coherently to find out if the instrument measures the same types of events over the mission.

The following thesis will give an understanding of the analysis of gamma-ray data from the INTEGRAL spacecraft and its astrophysical importance. Chapter 2 presents production mechanisms of gamma-rays (section 2.1) and their interaction with matter (section 2.2). Examples for astrophysical transient gamma-ray sources are given in chapter 3. The INTEGRAL spacecraft has two spectrometers, IBIS and SPI, whereas the latter and its surrounding anticoincidence shield are described in more detail in chapter 4. Chapter 5 demonstrates the extraction of information from the given data from the anticoincidence shield, for what the median filter is used as a background model (section 5.2.1). Additionally, an example for an observed gamma-ray burst with data from the anticoincidence shield is given (section 5.2.2) and Bayesian blocks are presented for a model independent analysis (section 5.2.3). Finally, the application of the upper method is shown in chapter 6 and at the end, a conclusion completes the thesis (chapter 7).

2 Gamma-ray production and interaction of gamma-rays with matter

The observation and detection of gamma-rays with INTEGRAL provides useful information about the most energetic phenomena in our Universe. In the following, explanations of gamma-ray production mechanisms and their interactions with matter are provided.

2.1 Gamma-ray production

High-energy photons can be produced in several processes such as radioactive decay, matter-antimatter annihilation or particle acceleration.

2.1.1 Radioactive decay

Radioactive decay is a spontaneous change of an atomic nucleus in form of a release of energy and matter from the nucleus. When there are more protons or neutrons in the nucleus, it becomes unstable, because the binding energy is not strong enough to hold the nucleons together and the nucleus decays by emitting particles. A decayed nucleus may be left in an excited state, which often de-excites by the emission of gamma-rays [3]. The decaying nucleus is called parent nucleus and the resulting nucleus is called daughter nucleus. In some cases, the daughter nucleus is unstable itself and decays again to a stable isotope by emitting more radiation.

The α-particle is composed of two protons and two neutrons and is the stable nucleus of ^{4}He. In a decay, the α-decay (figure 2.1), the parent nucleus ejects an α-particle with a following decrease in the atomic number Z by 2 and the mass number A by 4. The energy released in this process appears in form of kinetic energy of the ^{4}He nucleus and the daughter nucleus. As a consequence of momentum conservation, both the α-particle and the daughter nucleus must have equal but opposite momenta and thus have well-defined energies after the decay. The α-particle receives most of the kinetic energy, because of its smaller mass [4].

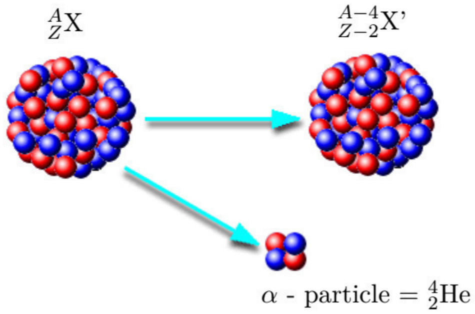

Figure 2.1: The α-decay. The parent nucleus X decays in a daughter nucleus X' with a decrease in the mass number A by 4 and the atomic number Z by 2 and an α-particle. Adapted from [5].

Another possibility for radioactive decay is the β-decay, where there are the β^+- and β^--decay that follow an excess of either protons or neutrons inside a nucleus (figure 2.2). In a β^+-decay a proton is converted into a neutron by emitting a positron and an electron neutrino in the process $p \rightarrow n + e^+ + \nu_e$. In a β^--decay a neutron transforms into a proton, an electron and an electron antineutrino through $n \rightarrow p + e^- + \bar{\nu_e}$. The positrons or electrons that are produced in a β-decay can annihilate with their anti-particles, if present, and convert their rest mass into photons of the energy 511 keV [6]. This matter-antimatter annihilation will be discussed in section 2.1.2. Mechanisms that produce β^+-unstable nuclei are explained in section 3.1. The β^+-decay is only possible inside a nucleus, because the mass of a free neutron is larger than the mass of a proton. In this process, electric charge and lepton number are conserved. In case of the conversion from a neutrally-charged neutron to a positively charged proton, a negatively charged particle, an electron, must be produced, too. Alternative to, and competing with the β-decay, a proton can capture an orbital electron from the atom, if a more stable nucleus results and convert into a neutron and electron neutrino: $p + e^- \rightarrow n + \nu_e$. This is called electron capture.

All three mechanisms change the proton number Z or the neutron number N, but the mass number A stays the same [4].

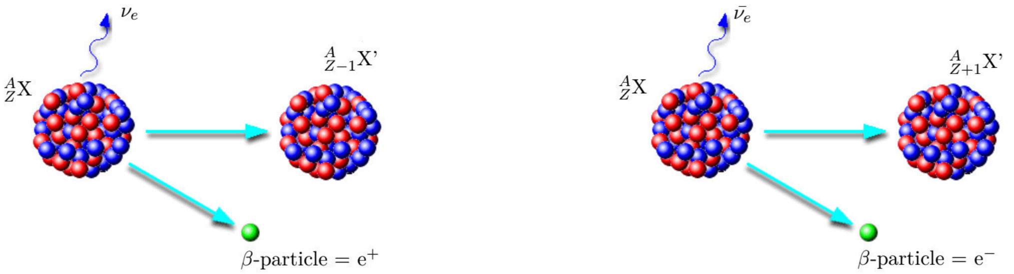

(a) The β^+-decay. A proton of the parent nucleus X converts into a neutron by emitting a positron and an electron neutrino.

(b) The β^--decay. A neutron of the parent nucleus X converts into a proton by emitting an electron and an electron antineutrino.

Figure 2.2: The β^+-decay (left) and the β^--decay (right) followed by an excess of either protons or neutrons inside a nucleus. Adapted from [5].

The process, which often occurs after α- or β-decays is the γ-decay. As shown in figure 2.3, an excited nucleus with higher energy de-excites to a nucleus with lower energy by emitting a high-energy photon [4].

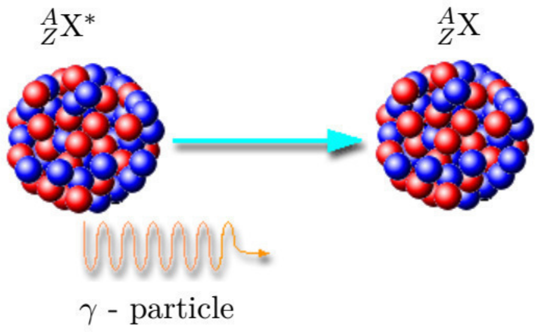

Figure 2.3: The gamma-decay. The excited nucleus X* de-excites to a nucleus X with lower energy by emitting a gamma-ray with discrete energy. Adapted from [5].

2.1.2 Matter-antimatter annihilation

In particle physics, every subatomic particle has an antiparticle. In case of the electron it is the positron, which has the same spin ($S = \frac{1}{2}$) and the same mass, but the opposite charge. These two leptons can interact in two different ways: they can either annihilate directly and form two photons, each with an energy of 511 keV or they can form a bound quantum state, called positronium, which decays, depending on the spin state, after a certain timespan. There are two states of positronium: ortho-positronium with parallel spins of electron and positron, and para-positronium with antiparallel spins. The para-positronium has a mean lifetime of 125 ps in vacuum and decays into 2 photons, each with an energy of 511 keV. The mean lifetime of the ortho-positronium is 142 ns and it annihilates through 3 photons, each with an energy of at most 511 keV, building a rising spectrum, with a sharp cutoff at 511 keV [7].

2.1.3 Acceleration of particles

Gamma-rays can also be produced through particle acceleration to nearly the speed of light, e.g. in shock waves of novae [6]. These particles are also recognized as cosmic rays, entering the solar system from outside. In the interstellar medium, they can interact with gas and produce secondary particles such as neutral pions π^0, for example. Pions are unstable and decay into gamma-ray photons of energy larger than 100 MeV/c^2 within a lifetime of 8.4 x 10^{-17} s via the electromagnetic force [8].

2.2 Interaction of gamma-rays with matter

There are three main mechanisms for gamma-rays to interact with matter: the Photoelectric effect, the Compton effect and pair production. For gamma-rays to be measured in a detector, these processes must be understood. In each of the processes, the energy of the photon is transformed into a measurable electric signal. Depending on the energy of the incident photon and the detector material, one of the processes dominates. [9].

2.2.1 Photoelectric effect

Before 1905, light was thought to be an electromagnetic wave. But then, Albert Einstein presented the idea of light being a particle, a discrete bundle of energy. Nowadays, light is treated like electromagnetic waves and also like particles. These particles, later called photons, are able to eject bound electrons from atoms. This effect is called the photoelectric effect and is illustrated in figure 2.4. Albert Einstein won the Nobel prize in 1921 for this effect.

The energy of a photon is given through the equation $E = h\nu$, where $h = 6.626 \times 10^{-34}$Js is the Planck constant and ν is the frequency of the photon [10]. The latter is related to the wavelength of the photon by $\nu = \frac{c}{\lambda}$, where $c = 299.792$ km/s is the speed of light [11]. When a photon interacts with an atom of the absorbing material, it transfers energy to one of its orbital electrons by being absorbed completely and sets this electron free [12]. This happens only if the energy of the photon is higher than the binding energy E_B of the electron. The minimum energy needed for setting an electron free is the work function of the material that is in the range of a few eV [12]. The resulting kinetic energy E_K of the photon after the interaction is $E_K = h\nu - E_B$ [9].

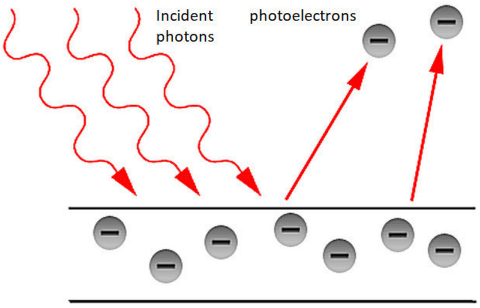

Figure 2.4: The photoelectric effect: the release of photoelectrons as a consequence of interactions of photons with an absorbing material. From [12].

2.2.2 Compton effect

In the early 1920s the Compton effect gave clear evidence for photons also having particle character. Arthur H. Compton described this effect as the increase of the wavelength of X-rays that are scattered by electrons in a carbon target. In general, this can be considered as inelastic scattering of photons by charged particles, which leads to a decrease of the photon energy, and thus to a larger wavelength of the scattered photons.

Figure 2.5 demonstrates the incident high-energy X-ray or gamma-ray that interacts with electrons of the target's atoms and transfers part of its energy to the electron. The electron is released from the outer shell of the atom and the scattered photon changes its direction. Because energy and momentum are conserved, the shift of the photon wavelength is determined by $\Delta\lambda = \frac{h}{m_e c}(1 - cos\theta)$. Here, $m_e = 511$ keV/c^2 is the electron mass and θ the scattering angle of the photon [13].

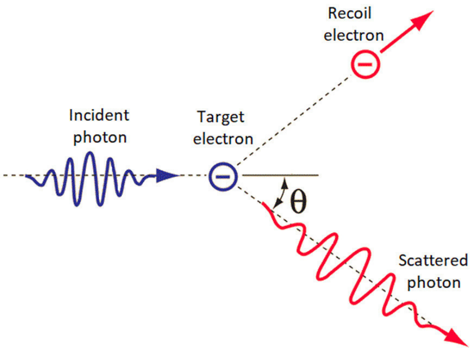

Figure 2.5: The Compton effect: inelastic scattering of a photon by a charged particle. From [13].

In astrophysics, the inverse Compton scattering is very important. Lower-energy photons are scattered by higher-energy relativistic electrons and so energy is transferred to the photon. This mechanism produces high-energy gamma-rays and can take place e.g. in the interaction of a Nova ejecta with a red giant wind [14] [6]. These astrophysical binary systems will be discussed in more detail in section 3.1.

2.2.3 Pair production

Pair production is a process, where a photon interacts with the Coulomb field of an atomic nucleus, for example, and produces an electron-positron pair. The schematic outline of this process is presented in figure 2.6.

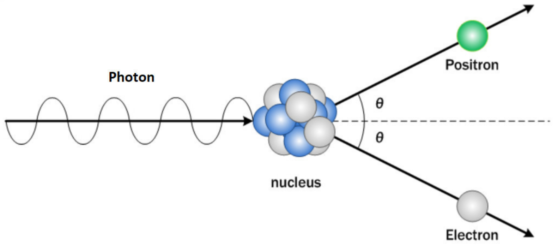

Figure 2.6: Pair production: the interaction of a photon with the Coulomb field of an atomic nucleus to produce an electron-positron pair. From [15].

The energy of the photon must be above a threshold of $2m_ec^2 = 1.022$ MeV to produce the two leptons. The presence of the nucleus is needed to conserve momentum [9]. The probability for this mechanism increases with increasing atomic number and increasing photon energy. Alternatively, the photon may also interact with the Coulomb field of an atomic electron (or free electron). In this case, the threshold energy for pair production is $4m_ec^2$.

3 Astrophysical transient sources

Transients are cosmic objects that occur on timescales of milliseconds to years. This is in contrast to the evolution of objects like galaxies or stars over millions to billions of years. Transient events can be very different and can be observed both in our own Solar System and outside, in our own galaxy or outside the galaxy [16]. Examples of such astrophysical transients, which can be observed also in gamma-rays, are neutron stars, novae and supernovae, black holes and active galactic nuclei, solar flares and gamma-ray bursts (GRBs) [2]. In this thesis, the focus is set on short gamma-ray transients, which could be measurable with the anticoincidence shield (ACS) of the spectrometer SPI aboard INTEGRAL (see section 4.2), i.e. up to a timescale of several hours. Therefore, in the following sections, novae (less than several hours), solar flares (up to minutes), and gamma-ray bursts (milliseconds to hours) are explained in detail.

3.1 Novae

The nova phenomenon can be explained as the ejection of nuclearly ignited material that has been accreted onto the surface of a white dwarf (WD). It is a star whose bolometric luminosity suddenly increases by a factor larger than 10^4 and then returns within a few months or years to its previous faint state [17]. In stellar evolution, stars with initial masses smaller that 8 $M_\odot$ - 10 $M_\odot$ end in compact objects with masses of typically $\sim$0.6 $M_\odot$ to a maximum of $\sim$1.4 $M_\odot$ which is the limiting Chandrasekhar mass. WDs are composed either of pure Helium (He), Carbon and Oxygen (CO) or Oxygen and Neon (ONe). If a single star evolves into a WD, i.e. without a companion, it will cool down as a consequence of unavailable nuclear energy until it is no longer seen. On the other hand, WDs in a binary system can either be totally disrupted in a type Ia supernova, or only their surfaces may ignite, which is called nova. In the latter case, there are two possible scenarios, depending on the companion star, which are explained below [6].

The first system is called a cataclysmic variable star which is a WD and a main sequence star as a companion that transfers hydrogen-rich matter onto the surface of the WD (figure 3.1a). The two stars have a distance of a few 10^{10} cm and an orbital period of hours to days. When enough matter is accreted on top of the WD, hydrogen burning sets in and a nova explosion occurs without a disruption of the WD because the outburst only affects the outer layers. The outburst happens as follows: hydrogen-rich matter is accreted from the secondary on top of the WD and forms a gas layer. The gravity of the star compresses the bottom of this layer and increases the pressure, so the material can not expand and becomes electron degenerate. This is a consequence of the Pauli exclusion principle that prevents two electrons to have the same quantum numbers [18]. In these extreme conditions, nuclear fusion can set in, and increase the temperature at the bottom of the accreted layer to a value of $\sim$7 x 10^7 K which is the Fermi temperature. A thermonuclear runaway is created. The material can expand and because of the very rapid increase of the temperature, material of 10^{-5} - 10^{-4} $M_\odot$ are ejected at large velocities of hundreds and thousands of km per second. After a few 10^4 to 10^5 years, a nova phenomenon can happen again as a consequence of repeated accretion of hydrogen-rich matter [17] [6].

The second scenario for a nova is a symbiotic binary with a red giant companion. An artist's impression of this type of nova is shown in figure 3.1b. The accreted matter comes from the red giant's stellar wind. The stars have a distance of 10^{13} - 10^{14} cm and the orbital period is in the range of a few 100 days. Because these novae are recurrent novae, frequent explosions with periods less than 100 years can be observed [6].

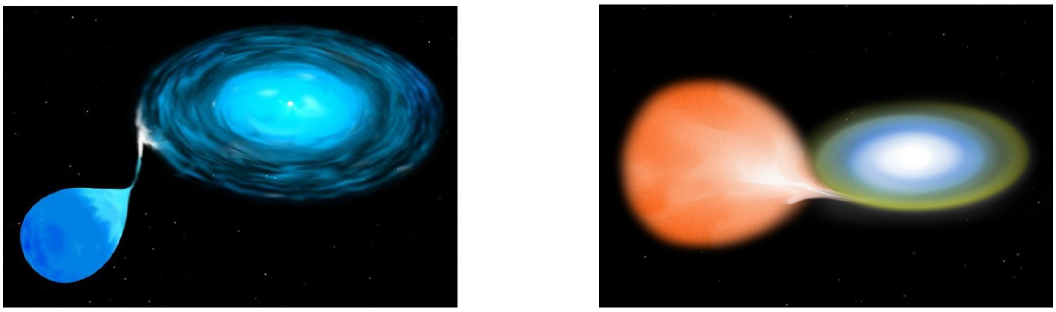

(a) Cataclysmic variable star with a WD and a main sequence star as a companion. From [19].

(b) Symbiotic binary with a WD and a red giant as a companion. From [20].

Figure 3.1: Artist's impressions of a cataclysmic variable star (left) and a symbiotic binary (right).

For both types of novae, during the hydrogen thermonuclear runaway, radioactive nuclei are synthesized that are β^+-unstable or experience electron capture and thus may emit photons with particular energies. The positrons emitted in a β^+-decay then annihilate with electrons and produce a photon with 511 keV and a continuum below this energy. Two main mechanisms produce β^+-unstable nuclei: the proton-proton (PP) chain which is important during the main accretion phase and the carbon-nitrogen-oxygen (CNO) cycle that produces energy for the thermonuclear runaway. The net effect of the PP chain is the fusion of four protons into one helium nucleus, two positrons, two neutrinos and gamma-radiation. One possible branch of the PP chain is the production of ^{7}Be through the fusion of ^{3}He and ^{4}He. The isotope ^{7}Be decays with a characteristic lifetime of 77 days by electron capture to ^{7}Li. This excited state of ^{7}Li then de-excites to its ground state by emitting photons with energies of 478 keV. This decay is expected predominantly for novae with the chemical composition of carbon and oxygen.

The CNO cycle begins with a reaction of a proton and a ^{12}C nucleus. This produces ^{13}N and a gamma-ray. The unstable ^{13}N β^+ decays to ^{13}C that captures a proton and converts to ^{14}N by emitting a photon. ^{14}N then captures another proton and becomes ^{15}O via the emission of a gamma-ray. ^{15}O converts to ^{15}N via the β^+-decay and finally, ^{15}N captures a proton and produces ^{12}C and a helium nucleus. The ^{12}C nucleus acts as a catalyst and is ready to re-enter the chain again [21]. The resulting CNO nuclei are transformed to ^{14}O and ^{17}F that emit positrons through proton captures. The three radioactive nuclei ^{14}O, ^{15}O and ^{17}F have very short lifetimes of 102 s (^{14}O), 176 s (^{15}O) and 93 s (^{17}F). These lifetimes are shorter than the time of the increase of the nova envelope transparency, so the photons that are released in the de-excitation of the radioactive nuclei can not escape.

There are two more major nuclear reaction cycles that produce radioactive nuclei: the NeNa cycle and the MgAl cycle. The first one synthesizes ^{22}Na that disintegrates to an excited state of ^{22}Ne that de-excites to its ground state by emitting energy of 1275 keV. The second one synthesizes ^{26}Al with a following decay to ^{26}Mg and a line emission at 1809 keV. The production of ^{22}Na and ^{26}Al is favored in ONe novae. The novae composed of CO and ONe show line emission at 511 keV that comes from electron-positron annihilation and also a continuum below this energy from the ortho-positronium decay. Those make the spectrum from 20 - 30 keV up to 511 keV, depending on the chemical composition of the nova envelope because of photoelectric absorption [6].

In gamma-ray astronomy, the light curve of a gamma-ray source is a useful method for the identification of this source. It shows the evolution of the photon emission in time. The following figure 3.2 shows the light curves of the 511 keV line for different CO and ONe novae models at a distance of d = 1 kpc:

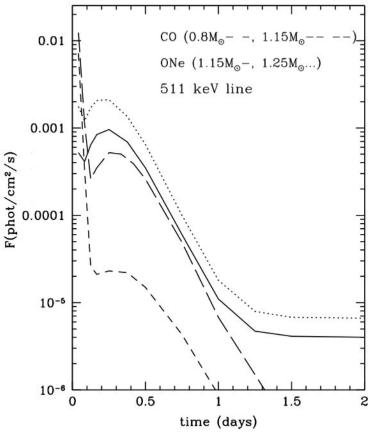

Figure 3.2: The 511 keV line light curves for CO and ONe novae with masses of 0.8 M$_\odot$ and 1.15 M$_\odot$ for CO and 1.15 M$_\odot$ and 1.25 M$_\odot$ for ONe at a distance of 1 kpc. From [6].

The high gamma-ray emission at the beginning of the nova comes from the decay of the two very short-lived radioactive nuclei ^{13}N and ^{18}F with lifetimes of 862 s and 158 min that emit positrons for the 511 keV annihilation line and the spectrum below this energy. The lower photon flux after ~1 day relates to the decay of ^{22}Na, in case of a ONe novae, and continues for about one week, because then the transparency of the envelope increases so rapidly that the long-lived ^{22}Na positrons with a lifetime of 3.75 years can escape into space without interacting with an electron. The short gamma-ray flash until 0.1 days is several magnitudes higher than expected for the above radioactive nuclei, so this means that a nova could be observed in gamma-rays earlier than in the optical band. Simulations show that the high photon flux from annihilation could possibly be observed for ~ 1 day and the lower photon flux for about one to two weeks, in case of ONe novae.

Also important are the light curves of the continuum below 511 keV of CO and ONe novae, presented in figures 3.3a and b, because the SPI Anticoincidence Shield can measure photons above 75 keV. Here again, simulations show a short flash that could be observed for 0.1 days.

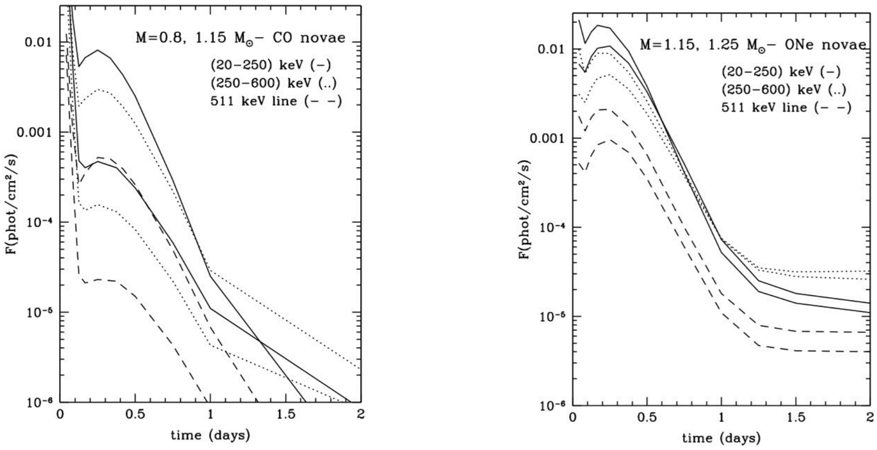

(a) Light curves of CO novae with masses of 0.8M $_\odot$ and 1.15M $_\odot$. The more massive novae have the higher photon fluxes.

(b) Light curves of ONe novae with masses of 1.15 M$_\odot$ and 1.25 M$_\odot$. The more massive novae have the higher photon fluxes.

Figure 3.3: Light curves of the continuum below 511 keV for CO novae (left) and ONe novae (right). The dashed line represents the 511 keV line for comparison. From [6].

3.2 Solar flares

The Sun lies in the centre of our solar system and influences not only the region inside the orbit of the outermost planet Neptune but also regions beyond this planet. The radius of the Sun is 696000 km and it consists mainly of hydrogen and helium [22]. Every second, energy of about 4 x 10^{26} J is emitted from the surface of the Sun into space. This energy is produced in the core, where hydrogen is fused to helium in nuclear reactions. This process is possible due to high pressure and high temperatures of 15 MK. One of the two main mechanisms for the production of β^+-unstable nuclei is the PP chain. It produces most of the energy of the Sun, and only 1 % is produced by the CNO cycle (section 3.1). The produced energy in the core region is then transported to the radiation zone, afterwards to the convection zone and finally to the photosphere. The latter is the visible surface of the Sun that is a few kilometres thick. From here, the Sun appears as a black-body with a temperature of 5700 K, for which it is classified as a G star [22]. Above the photosphere there are the chromosphere and the corona, the outer atmosphere of the Sun that can be seen by naked eye during a solar eclipse when the moon covers the Sun [23].

Sunspots are also part of the solar surface. They appear as dark, i.e. colder, regions of about 10000 km size. A picture of sunspots taken by the Solar and Heliospheric Observatory (SOHO) during a solar activity maximum in 2001 can be seen in figure 3.4.

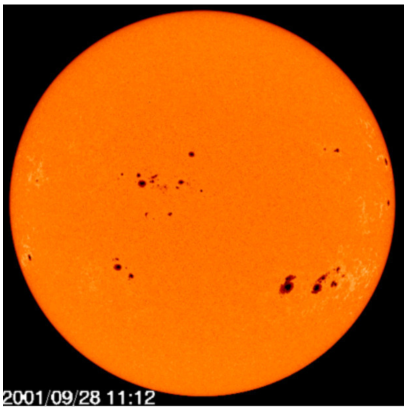

Figure 3.4: Sunspots on the surface of the Sun as visible phenomenon of the solar magnetic field during a maximum of solar activity in 2001, observed by the ESA & NASA Solar and Heliospheric Observatory SOHO. From [23].

Sunspots are created from the solar magnetic field and from a strong shear flow in the radiation zone and the convection zone. This shear flow causes different rotational periods of the surface of the Sun. The rotational period at the equator is 26 days and the one at the poles is 38 days. The magnetic field on top of the radiation zone is coiled and the strong shear flow intensifies it until it rises to the chromosphere and corona, where it can be seen as area of a concentrated magnetic field. There, the release of magnetic energy leads to particle acceleration that can be observed as solar flares that produce high-energy photons in the X-ray and gamma-ray band. The variation of solar activity (figure 3.5) can be observed in an eleven-year cycle (figure 5.2). At the end of a cycle, the number and size of sunspots reaches its maximum and the polarity of the Sun's magnetic field changes to the opposite. The spots last for typically a few weeks and originate at higher latitudes at the beginning of a cycle and then move to the equator [23].

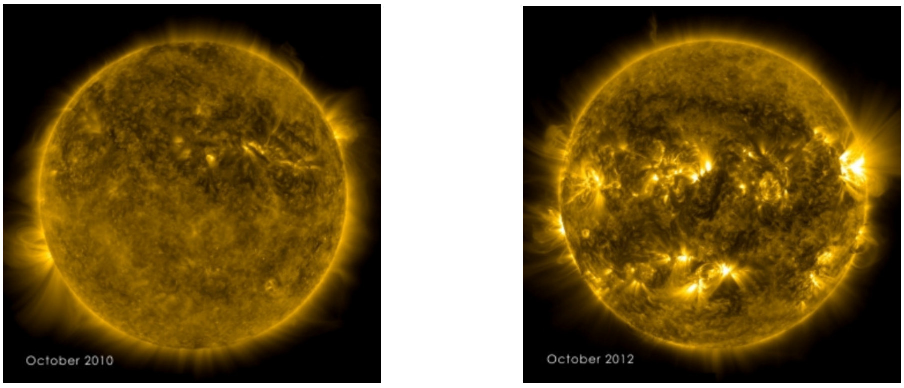

(a) The magnetic field structure of the corona, the outer atmosphere of the Sun, in a quiet time of solar activity in October 2010.

(b) The magnetic field structure of the corona in a more active phase of solar activity in October 2012.

Figure 3.5: The magnetic field structure of the corona at a minimum of solar activity in October 2010 (left) and a maximum in October 2012 (right), observed by the Solar Dynamics Observatory SDO. From [24].

The accelerated particles in solar flares interact with the Sun's atmosphere and produce line emission e.g. at 4.4 MeV from the ^{12}C de-excitation and 6.1 MeV from the ^{16}O de-excitation. These nuclei are produced in the CNO cycle that is explained in section 3.1.

As an example, the observed October 28, 2003 solar flare can be seen in figure 3.6. The ACS of SPI (see section 4.2) was very sensitive in this configuration for the detection of gamma-rays from the Sun because of its large effective area [25].

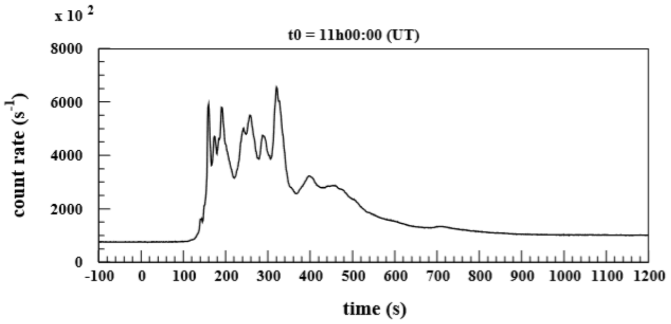

Figure 3.6: Total counts rate of the BGO ACS of the October 28, 2003 solar flare. A strong increase in the counting rate started at 11h02, followed by an intense phase with several narrow peaks and finally a decay phase sets in. From [25].

The count rate of the SPI ACS in figure 3.6 shows a strong increase at around 11h02. The most intense phase is accompanied by several narrow peaks, followed by a smoother decay phase [25].

3.3 Gamma-ray bursts

Gamma-ray bursts (GRBs) are short violent flashes of gamma-rays that come from any direction in the sky and last for tens of milliseconds to thousands of seconds. The origin of these phenomena can either be the merging of compact objects like neutron stars or black holes or the core-collapse of supermassive stars (8 $M_\odot$ - 130 $M_\odot$) [26]. Every GRB is followed by an afterglow, a long lasting emission of lower energy photons in the optical and X-ray band than can be observed hours to weeks after the explosion. Some gamma-rays interact with the external medium and radiation at longer wavelengths is produced. Differences in the afterglow can come from different total energies and different compositions of the ambient medium.

Binary neutron star mergers (figure 3.7a) are a progenitor for short GRBs. Another scenario is a neutron star-black hole merger, but this has not been confirmed yet. Those two compact objects merge because of the loss of orbital energy and angular momentum. A large amount of gravitational energy is released ($\sim 10^{54}$ erg/s) and also a small fraction of energy is liberated as particle jets in opposite directions that generate the GRB [27]. An illustration of the jets is shown in figure 3.7b.

The central engine of long and short GRBs is an accretion disk onto a black hole that can be formed differently in both binary mergers, neutron star-neutron star and neutron star-black hole. After the initial contact of two neutron stars, an object is formed within a few orbital periods that is quasi-axissymmetric and surrounded by a disk of material with a radius of tens of km and a density of $\sim 10^{11}$ - 10^{12} g/cm^3. The mass of the disk ranges from 0.03 $M_\odot$ to 0.3 $M_\odot$ for a system that has an initial mass of ~ 3 $M_\odot$. The initial mass has an effect on the merging process. If the mass is below ~ 2.6 $M_\odot$ a hypermassive neutron star, a neutron star supported by differential rotation, is formed. This star collapses to a black hole and a remaining disk of ~ 0.05 $M_\odot$ is formed through the transport of angular momentum to the matter surrounding the black hole. The second possible scenario is for initial masses above ~ 2.6 $M_\odot$. In this case and also if the mass ratio of the two neutron stars is below ~ 0.8, the central neutron star collapses into a black hole in less than 1 ms and leaves a very small disk, because it takes most of the mass with it. The disk of ~ 0.01 $M_\odot$ can then lead to a short GRB.

The formation of an accretion disk in a neutron star-black hole merger is less clear. The initial mass ratio $q \equiv M_{neutronstar}/M_{blackhole}$ is very important for the different evolution of the merging process. In case of $q \ll 0.1$, the neutron star falls into the black hole without being disrupted and no disk is formed. For an initial mass ratio of $q = 0.24$, 1/4 of the neutron star mass is transported outside the innermost stable circular orbit, which is in general relativity the orbit, where mass stably orbits a massive object and so, half of the mass is released, while ~ 0.15 $M_\odot$ remains bound. This matter builds a dense and hot disk that leads to a short GRB and after more than a second, a part of this matter ($\sim 0.05\ \mathrm{M}_\odot$) falls back toward the black hole after being ejected to eccentric orbits.

The duration of short GRBs lasts from 0.01 s to 1 s. This is the time for efficient accretion of hot and dense matter onto the black hole [28].

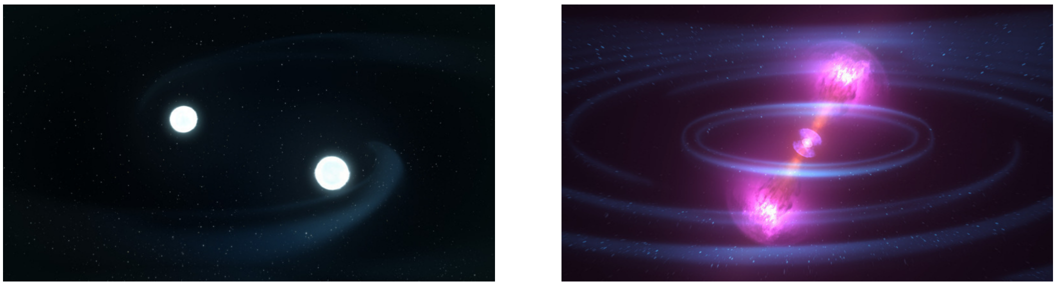

(a) Two neutron stars orbiting around each other as a progenitor for short GRBs. Orbital energy is released in form of gravitational waves that causes the neutron stars to move closer and finally merge.

(b) Relativistic particle jets after the merging process, producing a short GRB.

Figure 3.7: Illustrations of a binary system of two neutron stars before and after the merging process. From [27].

Long GRBs originate from the core-collapse of very massive stars to a black hole. They are also called 'collapsars' and can be observed in a gamma-ray emission from 1 s to 1000 s. Long GRBs release an enormous amount of energy ($\sim 0.001\ \mathrm{M}_\odot c^2$) in a region less than 100 km within seconds to minutes. This energy source leads to an acceleration of an ultra-relativistic outflow that can then be observed as prompt gamma-ray emission and a posterior afterglow (figure 3.8) [28]. Some long GRBs are thought to be supernovae, stars with initial masses above 8 - $10\mathrm{M}_\odot$ at the end of their stellar life. All stages of nucleosynthesis are completed, and no more binding energy can be produced. The stellar cores then become unstable, because the electrons that stabilize the core by electron pressure reach higher energies and can then be captured by nuclei. Afterwards, a gravitational collapse occurs within a second. The infalling matter reaches the core that leads to densities of $\sim 10^{13}\ \mathrm{g/cm}^3$. A shock is formed above the arising proto-neutron star. Neutrinos are produced from inverse β-decays and electron captures and heat the inner regions while some of the neutrinos can escape and cool the material. An instability sets in and a destruction of spherical symmetry results. Turbulences cause inwards and outwards gas flows [29].

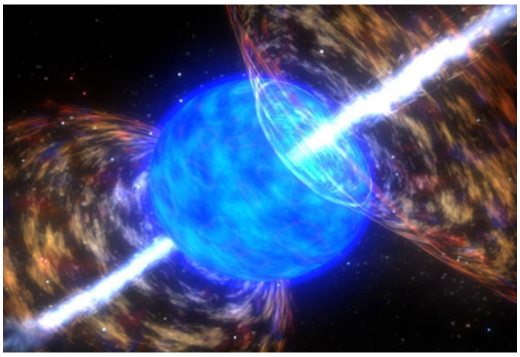

Figure 3.8: An illustration of a core-collapse of a massive star with the following relativistic jets along the star's rotation axis. From [30].

The lifetime of the accretion disk determines the duration of the GRBs. In case of short GRBs, the lifetime of the disk is expected to be a fraction of a second, whereas in long GRBs the matter from the collapsing star feeds the disk for a much longer time [28].

Figure 3.9 shows the T90 duration distribution of short (0.01 s to 1 s) and long (1 s to 1000 s) GRBs. The duration parameter T90 describes the time interval that begins with the detection of 5 % of the total measured counts of a burst and ends with the detection of 95 % of the measured counts [31].

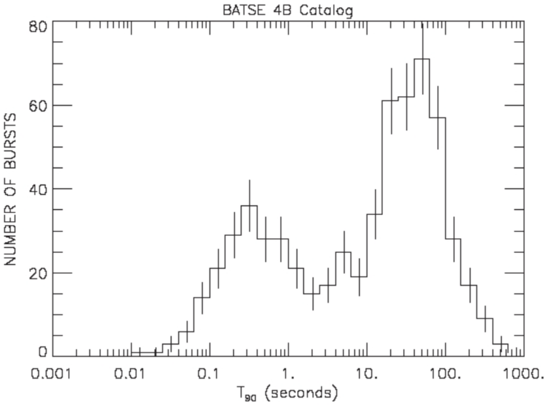

Figure 3.9: The T90 duration distribution of short and long GRBs, calculated with data from the Burst and Transient Source Experiment (BATSE) on board the Compton Gamma-Ray Observatory. From [31].

It is a bimodal distribution with a minimum around 2 s which means that GRBs can be classified in two sub-populations. Observations confirmed that the energy of short GRB photons is, on average, higher than the energy of long GRB photons [28].

4 The INTEGRAL spacecraft

The International Gamma-Ray Astrophysics Laboratory (INTEGRAL) is an ESA observatory within ESA's "Horizon 2000" programme and is supported by Russia and NASA. The idea for this scientific mission came from several international high energy astrophysicists and was presented to ESA in 1989. Four years later, in 1993, ESA approved the development, launching and a two year scientific mission that is extended every two years since then. In 2029, INTEGRAL is planned to re-enter into the Earth's atmosphere [29]. The INTEGRAL Science Working Team consists of Principal Investigators who lead the INTEGRAL Science Data Centre and payload complement, Mission Scientists and representatives of the participating international institutes from nearly all 14 ESA member states, USA, Russia, Czech Republic and Poland. During workshops in the development phase of the spacecraft in 1993, 1996, 1998 and 2000 the design of the mission operations and development of the data centre and payload was largely provided by the scientific community [2].

4.1 The INTEGRAL mission

INTEGRAL was launched from Baikonour in Kazakhstan on October 17, 2002 carried by a PROTON rocket from the Russian Space Agency. It was brought into a highly eccentric orbit with an apogee height of 154000 km and a perigee height of 9000 km. The duration of one revolution around the Earth is 72 hours with an inclination of 52.2 degrees. Scientific observations can be made for ≈90 % of the time of one revolution, while INTEGRAL is outside the Van Allen radiation belts, which are zones of energetic charged particles like electrons and protons, mostly of solar winds that are captured by the Earth's magnetic field [30]. The detection of gamma-rays of different astrophysical mechanisms is possible in the energy domain 15 keV to 10 MeV [2].

The spacecraft, shown in figure 4.1, has two main instruments, the spectrometer on INTEGRAL (SPI) with a field of view of 16° × 16° and the imager on board the satellite (IBIS) with a field of view of 9° × 9° and an energy range of 15 keV to 10 MeV [31]. SPI will be explained in more detail in section 4.1.1. Furthermore, two monitor instruments complement INTEGRAL, the coded mask X-ray telescope joint european X-ray monitor (JEM-X) in the energy range of soft and hard X-rays (3 keV - 35 keV) and the optical monitor camera (OMC) for exposing the observed sky regions in the energy range 500 nm - 600 nm [2] [32].

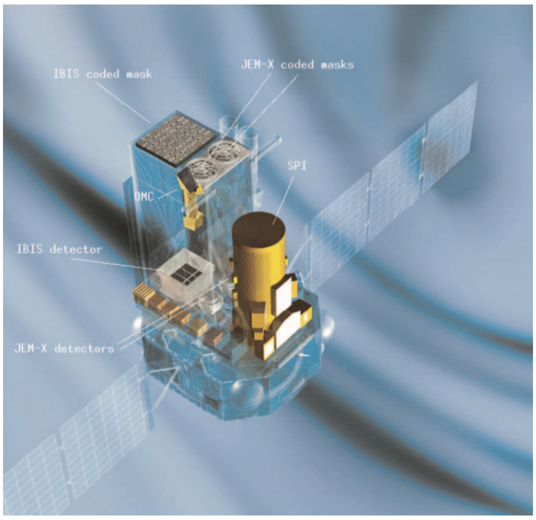

Figure 4.1: The INTEGRAL spacecraft with its two main instruments SPI and IBIS and its two monitor instruments JEM-X and OMC. The dimensions of the satellite are (5 x 2.8 x 3.2) m. From [2].

The goal of INTEGRAL is the physical study of the most energetic phenomena in our Universe that can be investigated by their gamma-ray emission. The instruments SPI and IBIS on INTEGRAL allow spectroscopy over a large energy range and also imaging and positioning of the gamma-ray sources within a large field of view can be provided by the instruments of INTEGRAL. Point sources can be distinguished from extended regions to identify the celestial gamma-ray sources. The line profiles and continuum of gamma-ray emission give information about the chemical composition and the inner and outer processes of different scientific objects, such as novae, for example. [2].

4.1.1 SPI

SPI enables high-resolution gamma-ray spectroscopy in the energy range of 20 keV to 8 MeV with an energy resolution of 2.5 keV at 1.3 MeV [32]. In this domain, gamma-rays of scientific objects such as GRBs, nova and supernova explosions, neutron stars or active galactic nuclei can be detected and investigated. SPI's field of view is $16^\circ \times 16^\circ$ with an angular resolution of 2.5°. In an area of 508 cm^2, 19 Germanium (Ge) detectors are arranged in a hexagonal array. This is the gamma-ray camera, the core of the instrument. An active cryogenic system continuously cools the detectors as they have to work at low temperatures of 85 K - 90 K. For imaging, there is a coded mask of tungsten blocks with a thickness of 3 cm above the Ge detectors to separate and locate celestial gamma-ray sources [32].

Cosmic ray interactions with the Ge detectors and the material around them cause a background that must be reduced to get a better sensitivity of the telescope. This can be reached with an active anticoincidence shield (ACS) consisting of BGO (bismuth germanate) crystals. In section 4.2 the ACS is described more precisely [32]. The following figure 4.2 presents the structure of SPI with the tungsten mask, the ACS, the plastic scintillator anticoincidence subassembly (PSAC) and the Ge camera.

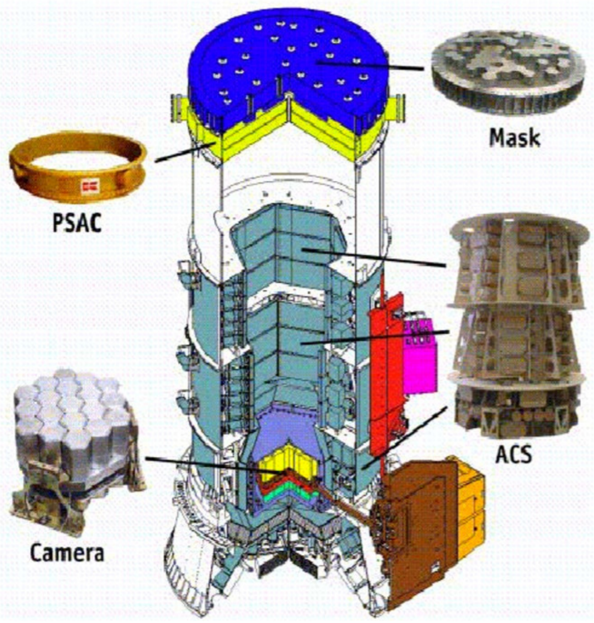

Figure 4.2: The SPI instrument with the tungsten mask for blocking parts of the field of view for separating and locating gamma-ray sources, the PSAC below it for reducing the background at 511 keV, the ACS consisting of BGO crystals for generating veto signals from charged particles and the 19 Ge detector camera. From [29].

The SPI mask (figure 4.3) with a weight about 140 kg is mounted 1.71 m above the Ge camera and consists of 127 hexagonal pixels. Gamma radiation can pass 64 of these pixels and the remaining 63 pixels are opaque to the photon flux within the energy range of SPI. The pattern of the coded mask has 120° symmetry and is arranged in a 720 mm diameter circle [32].

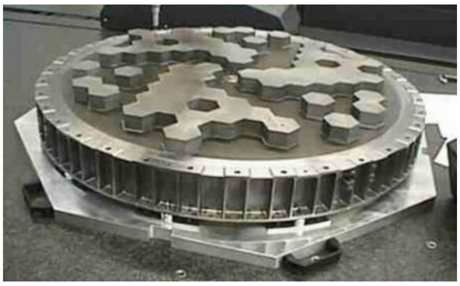

Figure 4.3: The SPI coded mask of tungsten blocks with 64 transparent pixels and 63 opaque pixels for imaging. From [32].

Furthermore, the background at 511 keV can be reduced by adding a plastic scintillator anticoincidence subassembly (PSAC) below the tungsten mask (figure 4.4). Because of a gap of 70 cm between the mask and the ACS, some particles do not reach the BGO ACS. This background of prompt interactions in the mask due to these particles can be reduced this way.

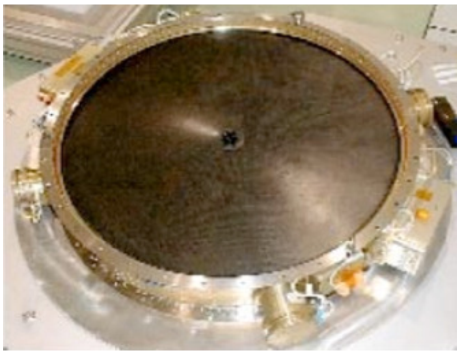

Figure 4.4: The plastic scintillator anticoincidence subassembly (PSAC) below the tungsten mask for reducing the background at 511 keV. From [32].

Figure 4.5 shows the camera of SPI that consists of 19 Ge detectors with a hexagonal shape. Each detector has a side length of 3.2 cm, a height of 69.42 mm, an external diameter of 60.65 mm, a distance of 56.04 mm from one flat side to the other and a distance of 6 cm from its center to the center of the neighbouring detector. The hexagonal shape minimizes the volume of the Ge detectors and the volume of the surrounding anticoincidence shield. The detectors are damaged by cosmic ray interactions but they can be restored by going through an annealing phase. There, the crystals are heated up to 105 °C, so that their structure can be re-arranged and to get a full recovering of the energy resolution. During the annealing phase, the data received from the ACS can not be used for scientific analysis. At the end, the detectors are switched on again before being cooled down to temperatures of 85 K by the cryostat, so consequently the received data must be treated carefully and are not easy to analyze [33].

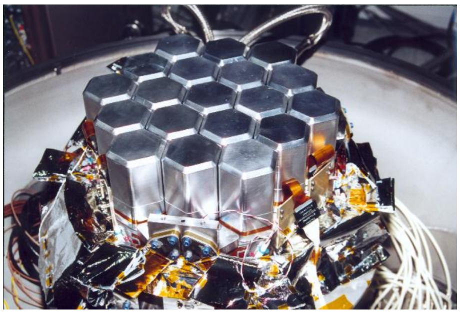

Figure 4.5: The 19 Ge detectors of hexagonal shape as the gamma-ray camera of SPI. From [34].

The cryostat has a mass of 80 kg and consists of four mechanical Stirling cycle coolers that are located on an external radiator. The Ge crystals have to be cooled to optimally 85 K for reducing the effect of radiation damage and getting higher timespans between successive annealings. A beryllium structure (Cold Box) at 210 K contains the detection plane, because the Ge crystals must be thermally insulated very well.

An onboard analysis of the data is made by the Data Processing Electronics (DPE) before it is sent to Earth. It receives all data from the Digital Front End Electronics (DFEE). Here, event building, classification and counting takes place and also veto signals are processed. The event timing of the system is 102.4 μs. The dead time that is the time after each event where SPI is not able to detect another event is monitored, too [32].

About every 30 minutes, INTEGRAL is reorientated with steps of 2.1 degrees. This 'dithering' strategy is used to follow a certain pattern to get images from different pointing angles to ensure unique coding information, and avoid degenerate pointing aspect angles if multiple sources are in the field of view. In this way, gamma-ray sources can be separated from the background [32] [29].

4.1.2 Other instruments aboard INTEGRAL

Besides the spectrometer SPI, a second gamma-ray instrument is mounted on INTEGRAL - IBIS, presented in figure 4.6. It works in the energy range 15 keV to 10 MeV and has a spectral resolution of 8 keV at 100 keV. Its fully coded field of view is 9° × 9° with an angular resolution of 12' [2].

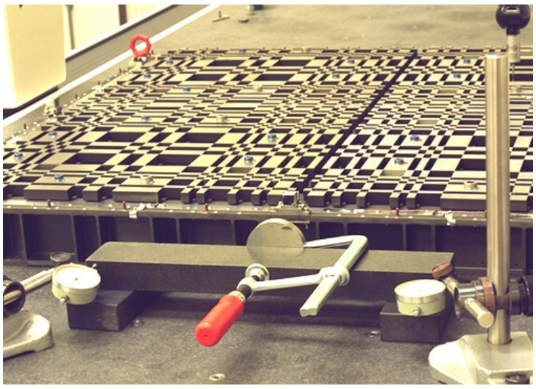

Figure 4.6: The IBIS coded mask. From [34].

The monitor JEM-X in the (3 - 35) keV X-ray band and the monitor OMC in the optical band at (500 - 600) nm are two more systems onboard the satellite and can be seen in figures 4.7a and b. JEM-X has a spectral resolution of 2.0 keV at 22 keV, a field of view of 4.8° with an angular resolution of 3'. The field of view of OMC is 5° x 5° and has an angular resolution of 25" [2].

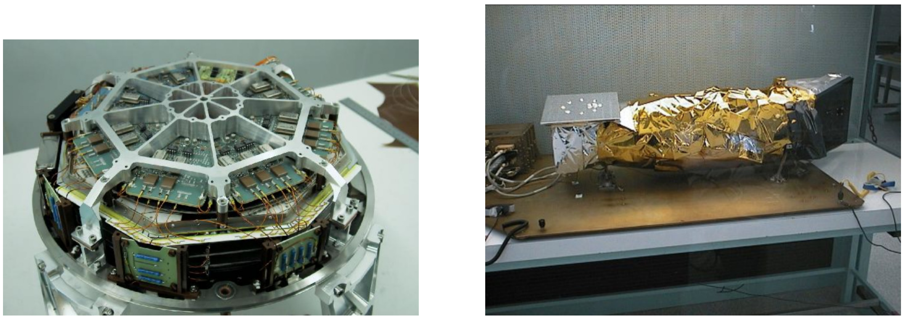

(a) The monitor instrument JEM-X. (b) The monitor instrument OMC.

Figure 4.7: The two monitor instruments JEM-X in the (3 - 35) keV X-ray band (left) and OMC in the (500 - 600) nm wavelength band (right). From [34].

4.2 The SPI Anticoincidence Shield

The large hexagonal anticoincidence shield (ACS) in figure 4.8 is an important part of SPI. This detector system encloses the entire instrument and consists of 91 BGO crystals with a total mass of 512 kg. Every crystal has a volume of ~790 cm^3 [32]. The Ge detectors are shielded by the ACS to reduce background radiation. The BGO crystals produce veto signals from charged particles that interact with SPI.

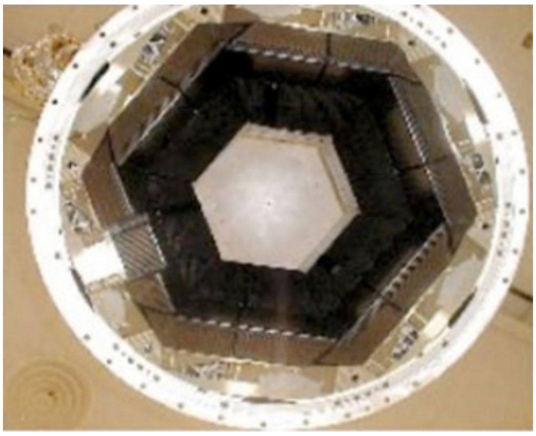

Figure 4.8: The large hexagonal anticoincidence shield as a veto system, consisting of 91 BGO crystals for reducing the background from prompt cosmic ray interactions with the Ge camera. From [32].

The BGO crystals are arranged in 4 subunits. The upper collimator ring (UCR) with a thickness of the crystals of 16 mm, the lower collimator ring (LCR) (figure 4.9a) and the side shield assembly (SSA) build the upper veto shield (UVS). Each of the systems has 36 crystals in a hexagonal array around the cylindrical axis of SPI. The lower veto shield

(LVS) has 36 crystals, too, that build a hexagonal shell but with a thickness of 50 mm [32]. Figure 4.9b shows the bottom section of the ACS.

The ACS has a time resolution of 50 ms, and measures photons above 75 keV. The effective area of the ACS provides an quasi-omnidirectional field of view, and thus does not have an angular resolution, because the direction of the incident gamma-rays can only be measured coarsely [35].

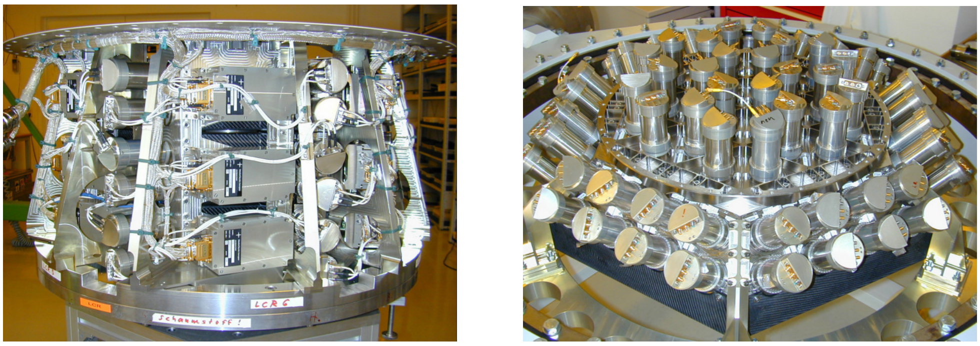

(a) The lower collimator ring (LCR) of the ACS.

(b) The bottom section of the ACS.

Figure 4.9: The lower collimator ring (LCR) (left) and the bottom section of the ACS veto system (right). From [34].

For not getting lost of a single BGO crystal of the ACS in case of a failure, each of them (with one exception) is viewed by two photomultipliers (PMTs) where one views different BGO crystals, in most cases neighbouring ones. These PMTs measure the scintillation light [29].

The anode signals always of two PMTs are summed of one of the 91 front-end electronic boxes (FEEs). Due to this method an uncertainty in the energy-threshold of the order of 100 keV of an individual FEE emerges, so that the threshold is unsharp. By considering the deadtime of SPI and the background reduction, the energy-threshold has a value of 75 keV [32].

4.2.1 Functionality of a Scintillator

The scintillator used in the ACS is BGO. It has a high density of 7.13 g/cm^3, so the short gamma-ray wavelenghts are not short enough to pass the crystal without colliding with electrons of the atoms to produce scintillation light [36]. Also, BGO is not self-absorbent for scintillation light and thus very efficient for gamma-ray absorption [37].

A scintillator is a material used to determine the energy and intensity of ionizing radiation that is radiation with high enough energy to release electrons from molecules or atoms through Compton scattering (section 2.2.2) [36]. During the transition of high-energy photons or charged particles through the scintillator, its molecules are excited and the electrons of the atoms are raised to an excited state with higher energy than the ground state. After some time, the atom returns to a lower energy state by emitting a photon. This photon has a characteristic energy with a peak at 480 nm in case of BGO [37].

The light is then multiplied by a PMT to get a stronger signal. The setup of a PMT is given in figure 4.10. A PMT is an electron tube with many parallel electrodes called dynodes, a photocathode at the beginning and an anode at the end. The incident photons from the scintillator strike electrons from the photocathode layer which are then focused by a focusing electrode and accelerated towards the first dynode. There, these photoelectrons strike more electrons, called secondary electrons. The dynodes produce an enormous amplification of each single incident photon up to 10^6. The anode at the end collects the electrons and a signal current can be measured [38] [39].

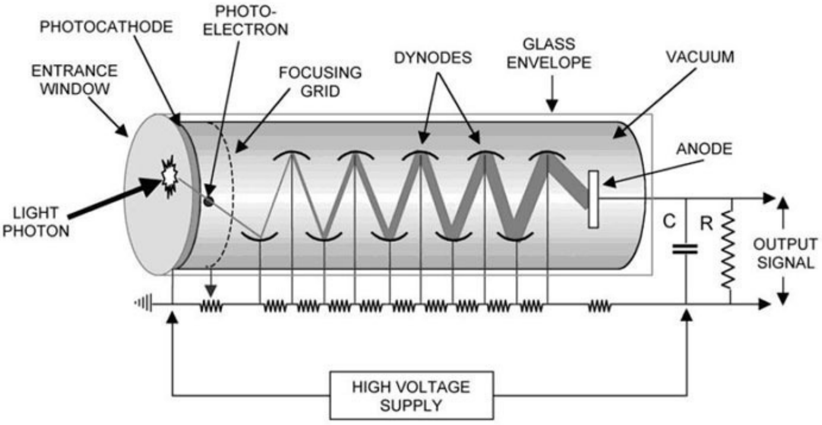

Figure 4.10: The setup of a photomultiplier for amplifying the signal of each incident light photon that passes a scintillator that is coupled on the left side. From [40].

4.2.2 The Anticoincidence Shield as sky monitor

The main task of the ACS is to generate a veto signal from charged particles and gamma-rays that come from outside the field of view. In this case, the Ge camera is turned off for 725 ns, so that in total only signals from inside the field of view are detected. However, the wealth of vetoed signals can be used to investigate prompt and short-duration emission from very energetic gamma-ray sources outside the field of view [29] [31] [32].

The geometrical area of the ACS is 3000 cm^2 to 8000 cm^2 for which the detection of gamma-ray bursts, for example, is possible [35]. However, the positional information is only coarse. For this reason, SPI ACS has been added to the 3rd interplanetary network (IPN) where burst locations can be determined down to the arcmin range [32]. The IPN collects data of several spacecrafts that can detect GRBs or other gamma-ray sources. The arrival time of the same burst is registered by different satellites and spacecrafts and in the following, the direction of the incoming gamma-rays can be found precisely through triangulation methods, demonstrated in figure 4.11. When three spacecrafts S1, S2, S3 detect the same burst, a line between two detectors D_{12} can be drawn that build an angle Θ with the burst direction. Then the burst arrives at S2 a timespan δT earlier than S1. The angle can be calculated through $cos(\Theta) = c\delta T/D_{12}$, where c is the speed of light. The solution of this equation is a ring or an annulus [41].

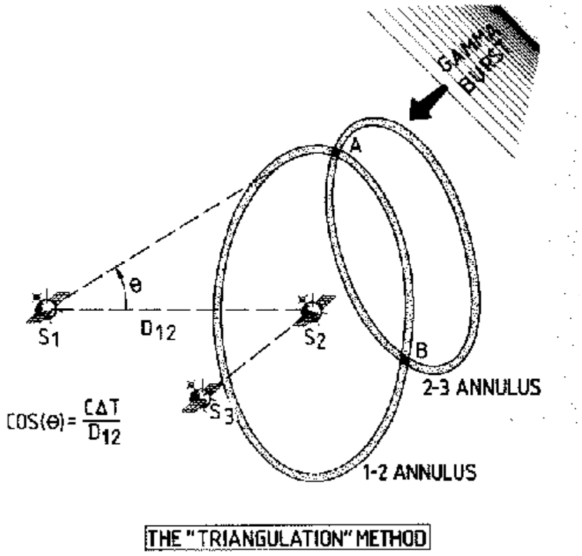

Figure 4.11: The triangulation method from the IPN for locating the direction of the incoming gamma-rays from a celestial source. From [41].

The expected values of observed GRBs per year with the ACS are ~ 50 bursts for 50 ms integration time and ~ 280 bursts for 1 s integration time. This was calculated with data from BATSE and PVO. For this measurement, the following assumptions were taken: the ACS background rate is between ~ 80000 counts/s and ~ 160000 counts/s, the detectable energy flux above 80 keV is 2 - 2.8 x 10^{-6} erg/cm^{2}s for a time binning of 50 ms and 5 x 10^{-7} erg/cm^{2}s for a time binning of 1 s [31].

5 Data analysis of gamma-ray light curves

The following chapter describes the variability in time, location and spectrum of the ACS count rate. For extracting information from these data, the background produced from interactions of charged particles with spacecraft material is explained. As a background model, the median filter of length 300 time bins is used and for model independent analysis Bayesian blocks are presented.

5.1 Data from the Anticoincidence Shield

The original data of the ACS are photons that interact with its BGO crystals and produce veto signals for the Ge detectors. The DFEE processes all received photon events from the ACS and the Ge camera and gives them to the DPE for an onboard analysis before sending them to Earth. This is explained in section 4.1.1. The ACS data vary in three categories: they vary in time, in location and in spectrum.

The variability of cosmic rays occurs on two timescales. When INTEGRAL enters the inner and outer radiation belt every 72 hours, charged particles like electrons and protons interact with the spacecraft and increase the photon flux due to radioactive decays within the instrumental material. This influences also the spectrum during orbital times outside the radiation belts, depending on the different life times of the material's atoms [29]. The passage through the radiation belts can be observed every three days in the ACS count rate in figure 5.1. During this time the instrument is switched off, so it can not be damaged by the high charged particle flux.

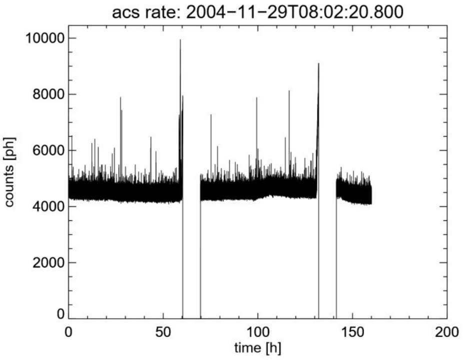

Figure 5.1: The count rate detected by the ACS on November 29, 2004 UTC 08:02:20.800. The passage through the radiation belts can be observed every 72 hours.

The second time scale is the annual one. The eleven-year cycle of solar activity, explained in section 3.2, has a great impact on the data from the ACS. The varying magnetic fields during the eleven-year cycle influence the production of solar flares that have their maximum at the maximum of solar activity. They irradiate the spacecraft with charged particles and neutrons, partly several times per day [29]. The maximum of the ACS rate, as seen in figure 5.2, is in November, 2009. At this time, the number of solar flares reaches its minimum and the magnetic field of the Sun is weak. This leads to a small shielding of the Earth from cosmic rays, so that the ACS count rate increases. It is anti-correlated to the solar cycle.

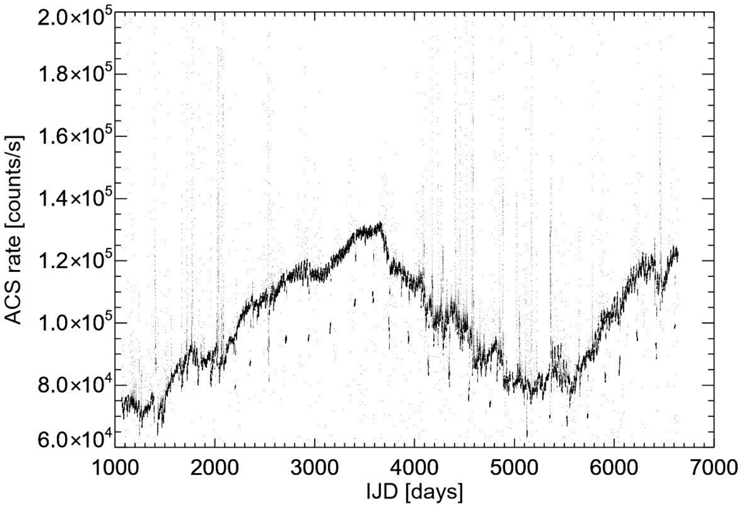

Figure 5.2: The evolution of the ACS count rate over the mission. The IJD time scale is in days with the beginning at IJD 1000 which is September 26, 2002 UTC 23:59:59.000.

There is also a local variability in the observed ACS count rate. The large effective area of the ACS, explained in section 4.2.2, can detect gamma-rays from all directions. The number of detected bursts and other gamma-ray sources depends on the one hand on the arrival angle of the gamma-ray flux. On the other hand, the spacecraft itself and also other spacecrafts can shield the photons. Also the Earth can shield gamma-rays if it lies in-between INTEGRAL and a celestial gamma-ray source [31].

For example, during the detection of the October 28, 2003 solar flare, Monte Carlo simulations show the configuration of INTEGRAL (figure 5.3) to the corresponding solar flare [42].

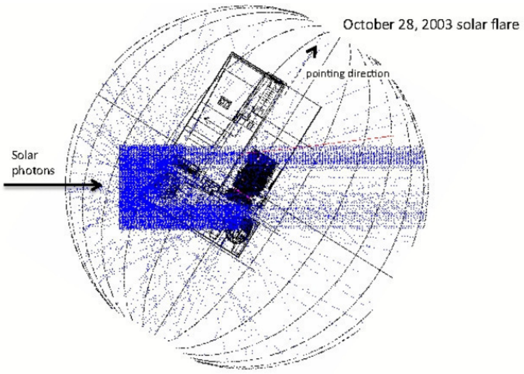

Figure 5.3: The configuration of INTEGRAL during the October 28, 2003 solar flare. The blue lines represent the solar photons and the red lines demonstrate secondary particles that are produced in the spacecraft material. From [42].

The third component is the spectral variability. Characteristic gamma-ray lines can originate from celestial sources and also from the spacecraft itself. They have a well-defined intensity and can be measured with the Ge detectors. Figure 5.4a and b show spectral lines near the annihilation line at 511 keV and near the ^{26}Al line.

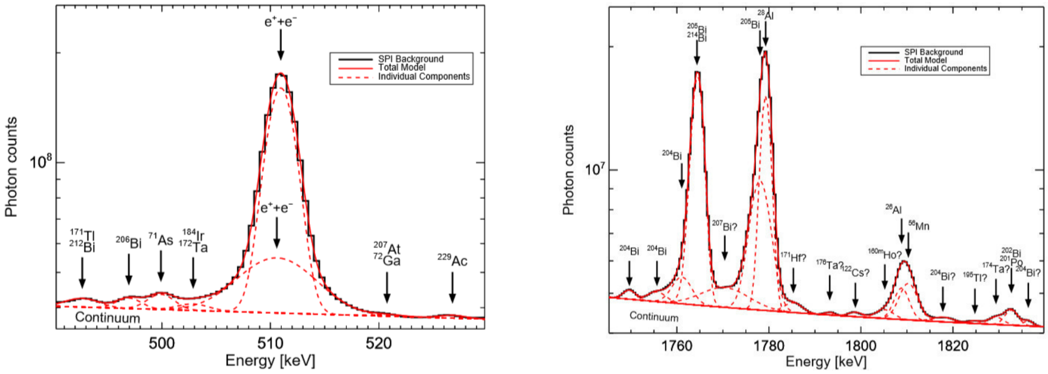

(a) The spectrum near the annihilation line of electrons and positrons at 511 keV.

(b) The spectrum near the ^{26}Al line.

Figure 5.4: The spectrum near the annihilation line of electrons and positrons at 511 keV and near the ^{26}Al line. The black lines demonstrate background from the SPI instrument, the red dashed lines are individual components and the red line represents the total spectral model. From [29].

The strong lines in figure 5.4b with peak energies at 1764 keV and 1777 keV come from electron captures of the element ^{205}Bi and the line at 1779 keV comes from a β^--decay of ^{28}Al. The spectral lines of Ga, As and Al in figure 5.4 are secondaries that originate from electron captures on ^{69}Ge, ^{68}Ga and ^{67}Ga. The background, produced by the spacecraft itself is constant in time, independent of its orientation in space [29].

For later analysis of data from the ACS, the Gaussian distribution is important. For a random variable X with mean x_0 and variance σ^2, the Gaussian distribution is a statistic distribution with the probability density function (PDF)

$$f_X(x) = A \cdot e^{-\frac{(x-x_0)^2}{2\sigma^2}}, \tag{5.1}$$

where A is the amplitude of the Gaussian function. The PDF describes the relative likelihood for a random variable X to be measured as a value x. The mean x_0, or the expected mean value, is the point, where the PDF has its maximum, i.e. the centroid of the distribution function. The variance σ^2 gives the dispersion of X around the mean value x_0, and σ describes the standard deviation of the mean value [43]. Applied on the ACS rate, this means that the measured counts per second fluctuate around a mean that varies between 80000 counts/s and 180000 counts/s.

Figure 5.5 shows the Gaussian PDF of four different values of the standard deviation σ = 0.4, 1.0, 2.2 and 0.7 and mean values of x_0 = 0 and -2.

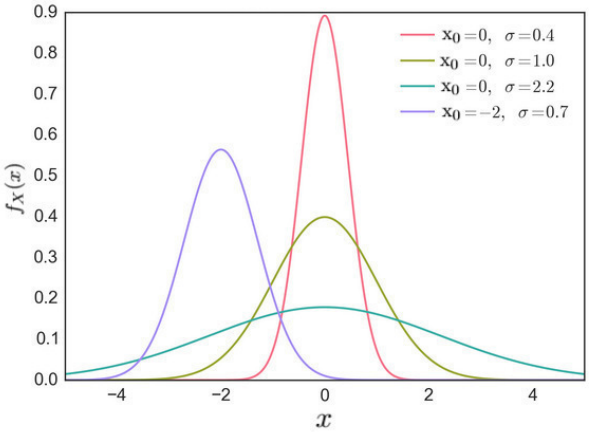

Figure 5.5: The Gaussian probability distribution function of four different standard deviation values σ = 0.4, 1.0, 2.2 and 0.7 around two mean values x_0 = 0 and -2. Adapted from [44].

In case of a mean value of $x_0 = 0$ and a variance of $\sigma^2 = 1$ the distribution is called standard normal distribution.

The probability that a random variable X is measured in a certain interval is given by calculating the integral of the PDF [43]. The probability for a variable X being in an interval $[x_0 - n\sigma, x_0 + n\sigma]$ with n = 1, 2, 3,... is

$$\int_{x_0-\sigma}^{x_0+\sigma} A \cdot e^{-\frac{(x-x_0)^2}{2\sigma^2}} dx = 0.68268 = 68.27\% \tag{5.2}$$

$$\int_{x_0-2\sigma}^{x_0+2\sigma} A \cdot e^{-\frac{(x-x_0)^2}{2\sigma^2}} dx = 0.95452 = 95.45\% \tag{5.3}$$

$$\int_{x_0-3\sigma}^{x_0+3\sigma} A \cdot e^{-\frac{(x-x_0)^2}{2\sigma^2}} dx = 0.9973 = 99.73\%. \tag{5.4}$$

The three-sigma rule says that there is a possibility of 99.73 % for a given event to be measured inside the region of normally distributed variables at a distance from the expected value (the mean value) to three times the standard deviation σ [45].

The probability for an event being measured in an interval of ± 5σ is 99,9999 % [46]. This threshold is important, because the probability for a measured count $\geq 5\sigma$ being statistical noise is very low.

The ACS is a counting experiment with the assumption that the measured count rate is Poisson distributed. The Poisson distribution has the following form:

$$f(n, \lambda) = e^{-\lambda} \cdot \frac{\lambda^n}{n!} \tag{5.5}$$

The parameter n = 0, 1, 2, 3, ... describes the number of events in a certain time interval and λ is the average number of events that is expected for each interval. The events must be random and independent of each other [47]. The parameter λ describes both the mean and the variance of the distribution, where the latter is the dispersion of a random variable X.

The following figure 5.6 shows the Poisson distribution for different values of λ.

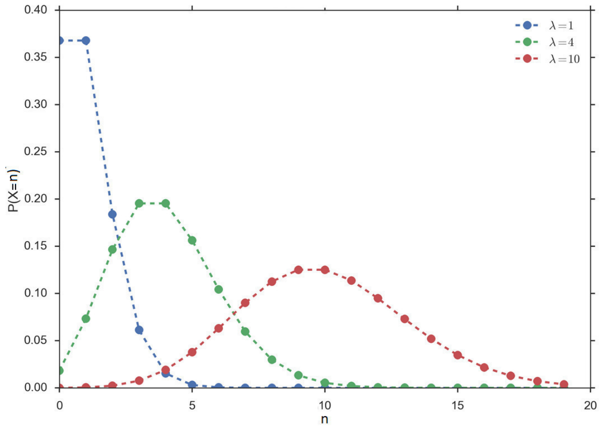

Figure 5.6: The Poisson distribution with different values of λ equal to 1, 4 and 10. Adapted from [44].

The shape of the Poisson distribution changes with different values of λ. For small values the distribution has a tail that extends to the right to larger values. For higher values, the distribution is more spread and looks symmetric [48]. For very large values of λ ($\lambda \to \infty$) the Poisson distribution approximates the Gaussian function [47]. The expected statistical fluctuations of a measurement of n counts are estimated as $\sqrt{n}$. This is sometimes called a statistical error of the measurement; properly speaking, it is the uncertainty of the measured value under statistical fluctuations, if the true value would be n counts.

5.2 Extracting information

The data that we use in this thesis are counts recorded by the ACS system. They are used to veto signals seen in the Ge detectors, because the ACS triggers mostly on cosmic ray interactions, which are 'background' for the Ge detectors when trying to measure cosmic photon events. As a consequence of this, the data are a superposition of signal photons ('signal') from celestial gamma-ray sources and background photons ('noise') from either cosmic gamma-rays or interactions of charged particles with instruments of the spacecraft [33]. As an example, figure 5.7 presents the ACS rate obtained from January 1, 2011 UTC 00:00:00.000. The detected counts can either be signal or noise, whereas the origin of noise is explained below.

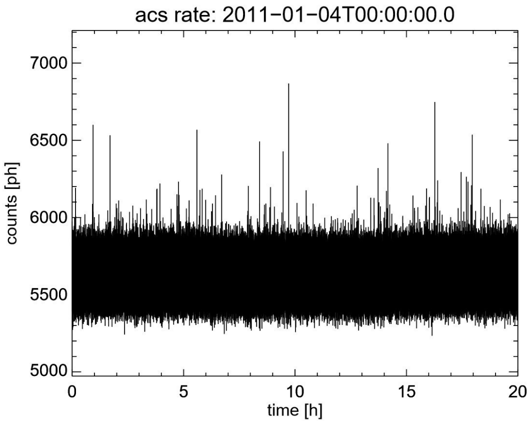

Figure 5.7: The measured count rate of the ACS on January 1, 2011 UTC 00:00:00.000. The x-axis shows the time in hours and the y-axis shows the count rate per 50 ms time bins.

Three components contribute to the background: the continuum background, the 511 keV background and the background from gamma-ray lines. The continuum background comes from outside the spacecraft, from the cosmic diffuse gamma-ray flux that hits the instrument and passes the BGO ACS because of leakage. The 511 keV background can originate, for example, from unstable nuclei in the materials of the ACS, the Ge detectors or the cryostat that are produced through interactions of charged cosmic ray particles with the atoms of the instrumental materials. The β^+-unstable nuclei decay and produce positrons that annihilate with electrons and produce photons of 511 keV.

The third background influence is from gamma-ray lines. For example, germanium and bismuth of the BGO crystals can decay, producing characteristic lines, for example, at 872 keV and 1107 keV in case of germanium and 1764 keV in case of bismuth. When charged high-energy particles interact with nuclei of the instrumental material, they can generate radiation processes that produce secondary particles, protons and neutrons, and also excited nuclei that de-excite to their ground state by emitting photons, causing delayed background emission lines. Prompt emission comes from bremsstrahlung, from secondary particles, and electromagnetic nuclear transitions from higher nuclear energy levels to the ground state [33] [29].

For the analysis of the ACS count rate, different data sets can be used. The size of a single time bin in the ACS rate is 50 ms. Consequently, 1 s contains 20 bins, 8 s contain 160 bins and one minute is made of 1200 bins. If the purpose now is to search for events with a longer duration than 50 ms, e.g. long GRBs, the time and the counts can be rebinned to simplify the analysis of longer data sets. This means that for a bin factor of 20, for example, always 20 entries in both time and count rate array are summed and normalised to the bin factor itself. At the end of the rebinning, the initial array is reduced to a new array with less entries.

The following figures 5.8a and b show 20 hours of the ACS rate from January, 1 2004 UTC 00:00:00.000. Before the rebinning process to a one second time binning, the time array contains 1440000 bins which is 20 hours. After the rebinning, the new time array contains 72000 bins.

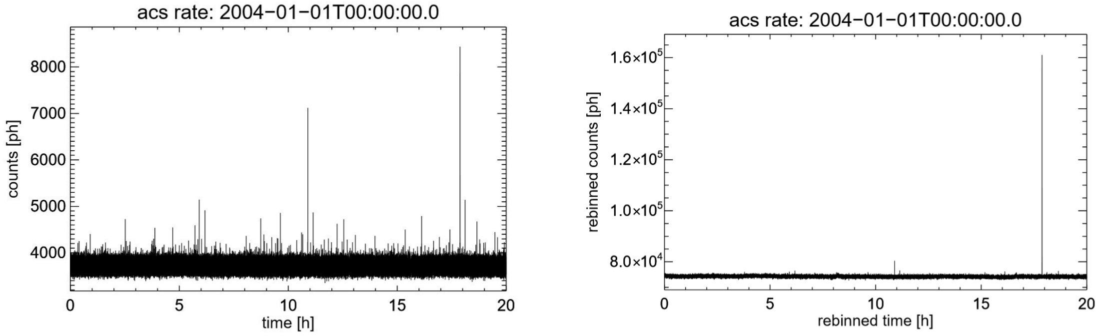

(a) The measured count rate detected by the ACS on January 1, 2004 UTC 00:00:00.000.

(b) The rebinned count rate detected by the ACS on January 1, 2004 UTC 00:00:00.000 binned to a one second time binning.

Figure 5.8: The measured count rate detected by the ACS on January 1, 2004 UTC 00:00:00.000 before (left) and after (right) the rebinning of time and counts to a one second time binning. The normalisation of the total counts is then the bin factor itself and the initial time array is reduced from 1440000 bins to 72000 bins.

Due to the specific illustration of the rebinned data in figure 5.8b, less peaks can be seen. They demonstrate events with a duration of 1 s. The following plot 5.9 gives a comparison of the obtained data (black) and the rebinned data (red). Marked in blue is the maximum value of the measured count rate.

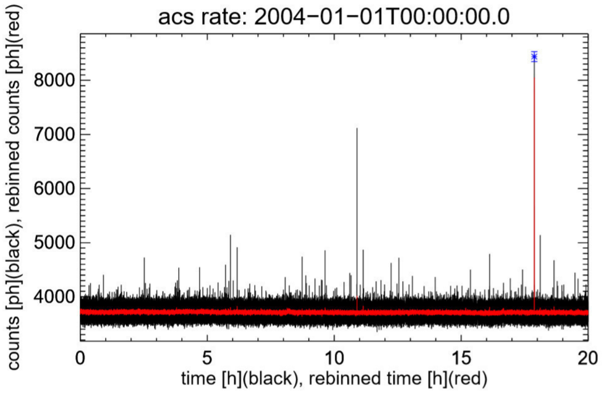

Figure 5.9: The count rate (black) compared to the rebinned count rate to a one second time binning (red) and the maximum value (blue) obtained from the ACS on January 1, 2004 UTC 00:00:00.000.

Examples for the rebinning of time and counts to an 8 second time binning is given in figure 5.10. Shown is the ACS rate on November 29, 2004 UTC 08:02:20.800. This figure is also presented in section 5 to demonstrate the 72 hour orbital time of INTEGRAL. The rebinning of these data to an 8 second time binning is given in figure 5.10b.

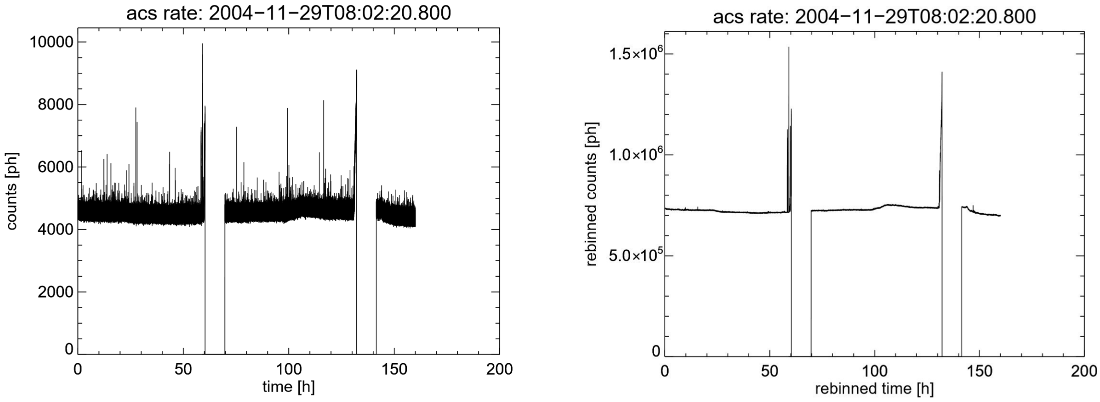

(a) The measured count rate of the ACS on November 29, 2004 UTC 08:02:20.800.

(b) The rebinned count rate to an 8 second time binning of the ACS on November 29, 2004 UTC 08:02:20.800.

Figure 5.10: The measured count rate of the ACS on November 29, 2004 UTC 08:02:20.800 before (left) and after (right) the rebinning of time and counts to an 8 second time binning. The normalisation of the total counts (right) is the bin factor itself.

The two figures 5.10a and b can also be shown in one figure (figure 5.11) for comparing the data with the rebinned data.

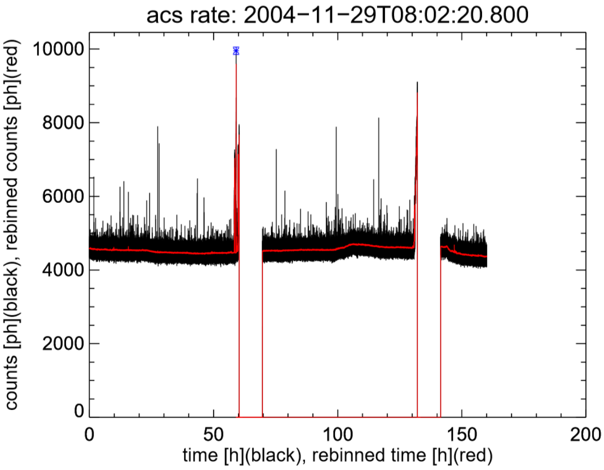

Figure 5.11: The measured count rate (black) on November 29, 2004 UTC 08:02:20.800 compared to the rebinned count rate to an 8 second time binning (red) and the maximum value (blue).

A one minute time binning can also be made. For example, this is applied to the measured count rate of the ACS on January 1, 2006 UTC 00:00:00.000 (figure 5.12). The measured data and the rebinned data are pictured in figure 5.13. The strong increase of the measured count rate in the range of $\sim 3 \times 10^5$ to 5×10^5 counts every 72 hours in figure 5.12a represents the entering of INTEGRAL in the Van Allen radiation belt.

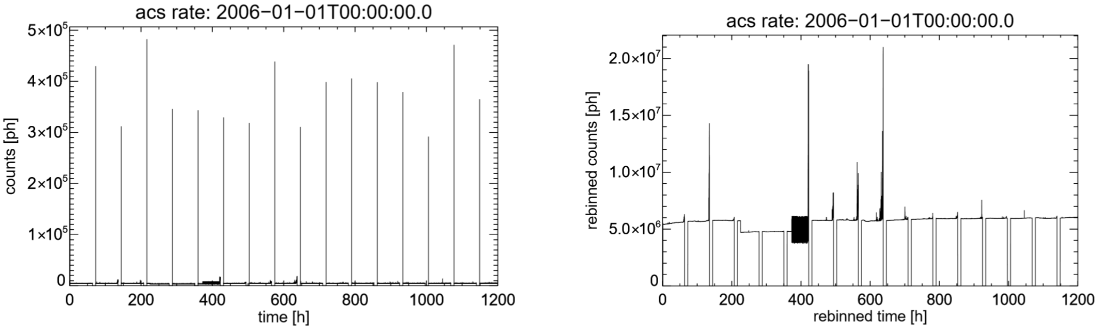

(a) The measured count rate detected by the ACS on January 1, 2006 UTC 00:00:00.000.

(b) The rebinned count rate to a one minute time binning detected by the ACS on January 1, 2006 UTC 00:00:00.000.

Figure 5.12: The measured count rate detected by the ACS on January 1, 2006 UTC 00:00:00.000 before (left) and after (right) the rebinning of time and counts to a one minute time binning. The normalisation of the total counts (right) is the bin factor itself.

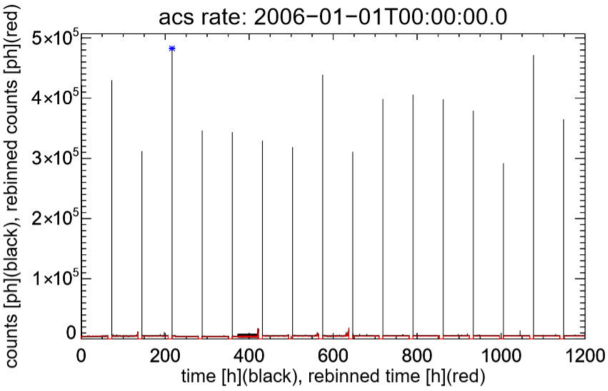

Figure 5.13: The measured count rate (black) on January 1, 2006 UTC 00:00:00.000 compared to the rebinned count rate to a one minute time binning (red) and the maximum value (blue).

For extracting information from the given data, robust algorithms must be applied to distinguish between an 'uninteresting' background and possible additional photon counts from celestial gamma-ray sources. The robustness is the strength of a statistical model or procedure. This means that even if the conditions are not exactly met, correct results may be provided from the model [49]. A robust algorithm must make use of the statistical fluctuations and the modeling of the signal, to derive the results that are most probably supported by the measurement. A most-advanced such method is the Bayesian approach discussed below. A possibility for empirically modeling the background is by using a median filter, which will be explained in the next section 5.2.1.

5.2.1 The median filter as a background model

A good background model is one that extracts information best without losing the sensitivity for the detection of celestial gamma-ray sources. As already discussed in section 5.2, the measured ACS counts are dominated by veto signals from cosmic ray interactions with the BGO scintillators, and internal gamma-ray emission from lines and continuum, that may also trigger the ACS. We chose to split our data into an 'uninteresting' part that varies on longer timescales, and an 'interesting' part that varies on shorter time scales. The former may arise from orbital cosmic ray exposure variations, and we might call this 'background'. The latter may arise from gamma-ray bursts or other cosmic explosions or transients, and we may call this 'signal'. The background has to be determined in an unbiased way from the data itself, because predictions of cosmic-ray interactions with the ACS are not possible, and no universal background model for the ACS rate is available. It is now important to subtract the background from the data to get the signals from short-duration transient phenomena like novae, gamma-ray bursts or solar flares. By considering the count statistics to be Poisson-like, a viable method to estimate the background contribution in a given light curve is by applying a median filter. For a given length (duration) of such a filter, transient events of this time scale or shorter can be identified.

Consider a sequence of numbers, e.g. measured counts per unit time, data = [2,3,1,3,2,50,3]. Now, by sorting the numbers numerically from the smallest to the largest, the new array appears as [1,2,2,3,3,3,50]. The median, in general, is the central value, which is 3 in this case. For an odd number of array entries, the median is the mean value of the two central entries. Additionally, the median can also be taken from a fixed number of entries, which would be the length of the filter, m. For example, in case of a median filter m = 3, the first two numbers and the first number that is repeated are sorted which leads to [2,2,3] with a median value of 2. At the boundaries of a sequence of numbers, there are no entries, so the first and last value are repeated for obtaining enough entries to fill a certain median filter. The second step is the numerically sorting of [2,3,1], where the resulting median value is 2. The next three entries are [3,1,3] with the following median of 3. This process goes through all array numbers until the last three entries [50,3,3]. The last median value then is 3. At the end, the initial array transforms to [2,2,3,2,3,3,3]. In this data set, the peak number (50) is removed.

The two figures 5.14a and b demonstrate a median filter of length 300 time bins, which is equal to 15 seconds, as a background model applied on the ACS data of January 3, 2003 UTC 02:02:20.800.

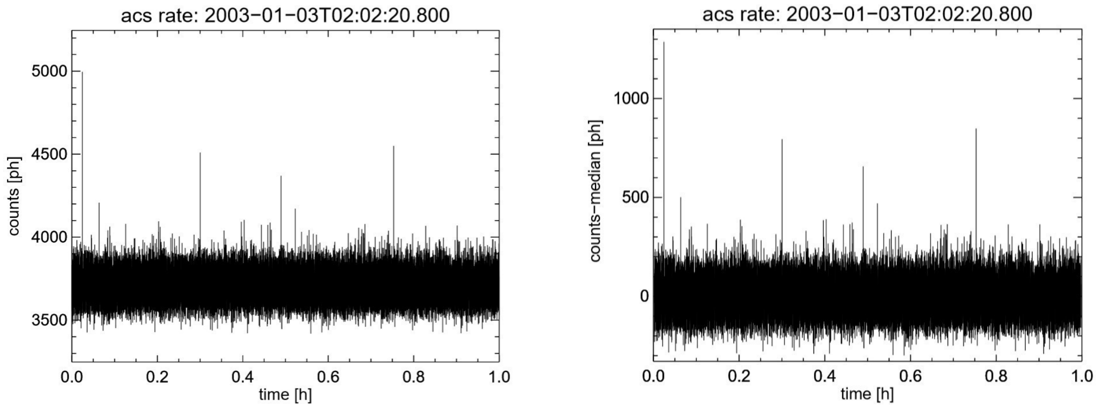

(a) The measured count rate of the ACS.

(b) The measured count rate of the ACS minus the median filter as background model.

Figure 5.14: The measured count rate of the ACS on January 3, 2003 UTC 02:02:20.800. The left figure shows the obtained data from the ACS and the right figure shows the new data after subtracting the background from the data. The background model is a median filter of length 300 time bins, which is equal to 15 seconds.

In the same way to the case of the smallest bin size, the median filter can now be applied to also the rebinned data set. Similarly, the residuals of the rebinned counts are shown in figure 5.15. As expected from subtracting a background model, the residual counts scatter around 0, with positive excesses due to possible celestial signals.

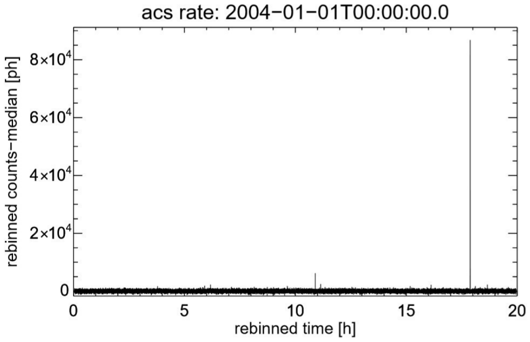

Figure 5.15: The rebinned data to a one second time binning minus the background as a median filter of length 300 time bins, obtained from the ACS on January 1, 2004 UTC 00:00:00.000.

For the rebinning to an 8 second time binning of the data in figure 5.10b and a one minute time binning of the data in figure 5.12b, the applied median filter is illustrated in figure 5.16a and b.

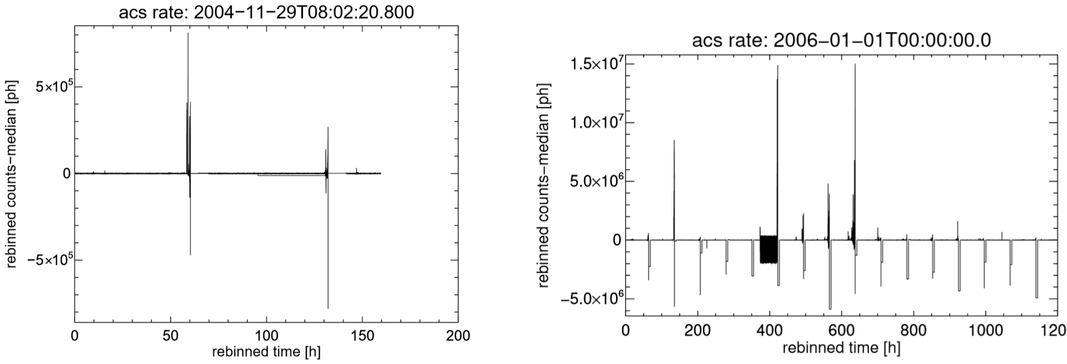

(a) The rebinned data to an 8 second time binning minus the background as a median filter of length 300 time bins, obtained from the ACS on November 29, 2004 UTC 08:02:20.8000.

(b) The rebinned data to a one minute time binning minus the background as a median filter of length 300 time bins, obtained from the ACS on January 1, 2006 UTC 00:00:00.000.

Figure 5.16: The rebinned data to an 8 second time binning (left) and to a one minute time binning (right) minus the background as a median filter of length 300 time bins, obtained from the ACS on November 29, 2004 UTC 08:02:20.8000 and January 1, 2006 UTC 00:00:00.000.

The residuals of the rebinned counts are also scattered around 0 after subtracting the background and have several positive values that can come from celestial gamma-ray sources.

The subtraction of the background from the data provides the residuals, which can be analyzed in further steps. These residuals are then analysed for consistency and extra components. This is done by normalising the residual counts, R = D - M, to the expected statistical fluctuations of the data, estimated as $\sqrt{D}$, and counting the individual entries for a distribution function. This is visualised in a histogram, which is a type of bar plot that counts the number of events that fall into a given interval. The bin size is chosen as 0.125. The x-axis in the histograms is calculated through (D$_{rebinned}$ - M)/$\sqrt{D_{rebinned}}$.

For example, a histogram of the residuals of the measured and analyzed count rate of January 3, 2003 UTC 02:02:20.800 is shown in figure 5.17.

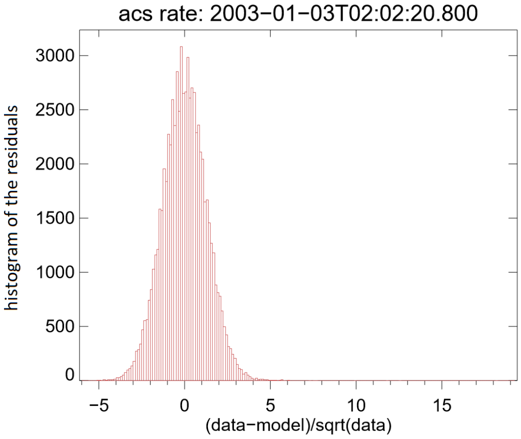

Figure 5.17: The histogram of the normalised residuals, obtained from the ACS on January 3, 2003 UTC 02:02:20.800. The median filter has a length of 300 time bins, and the bin size is 50 ms.

For a high number of events in each interval, this histogram can be superimposed with a Gaussian function (figure 5.18) that is explained in section 5.1. The superposition shows the distribution of the measured counts, where the background is presented by values inside the curve, and the significant part of the data is outside the curve.

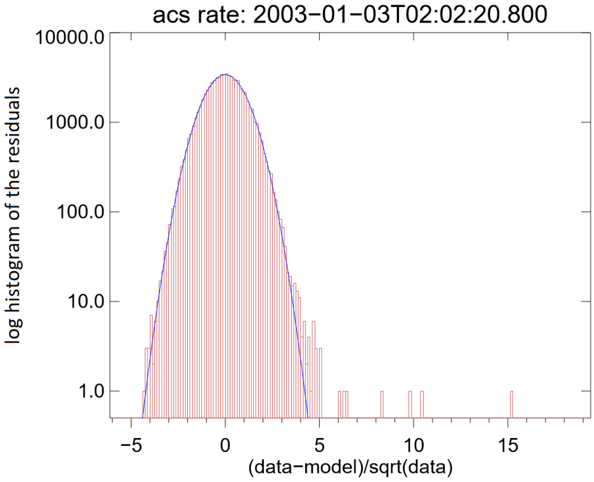

Figure 5.18: The logarithmic histogram of the residuals with a superimposed Gaussian function.

The superimposed Gaussian function has a standard deviation of σ = 1.2 instead of $\sigma = 1$. This means that the initial assumption of Poisson distributed data and its statistical error in form of the square-root of the data, as explained above, is not correct. The statistical errors are too small for the data of the ACS, so they must be multiplied by a factor 1.2.

The Gaussian function describes the distribution of the negative values very well, which means that the median filter is a good background model. We adopt the Gaussian to represent our 'uninteresting' background signal and its fluctuations; hence the part not included in the Gaussian distribution constitutes the 'interesting' part of the data. We chose to only report particularly-large deviations from the Gaussian, i.e. several times its intrinsic width measured by σ. Significant values that are those with standard deviation larger than 5σ, for example in figure 5.18, can be marked in the ACS count rate with the subtracted background in figure 5.19.

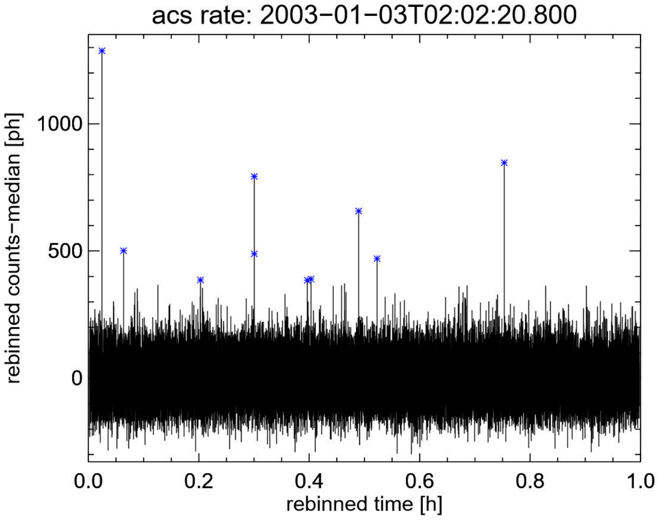

Figure 5.19: The measured count rate of the ACS on January 3, 2003 UTC 02:02:20.800 with a bin size of 50 ms. Significant counts are marked in blue.

The residuals of the rebinned counts to a one second time binning of January 1, 2004 UTC 00:00:00.00 in figure 5.15 can also be plotted in a logarithmic histogram (figure 5.20a) and the signals above 5σ are then marked in figure 5.20b.

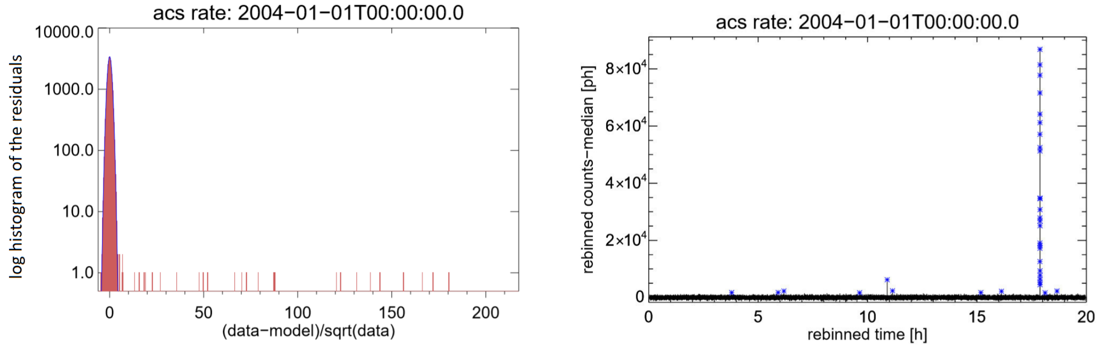

(a) The logarithmic histogram of the residuals with a superimposed Gaussian function.

(b) The rebinned count rate to a one second time binning.

Figure 5.20: The measured count rate of the ACS on January 1, 2004 UTC 00:00:00.000. The data are rebinned to a one second time binning and a median filter of length 300 time bins is used. The left figure shows the logarithmic histogram of the residuals and a Gaussian function. The right figure shows significant counts, marked in blue.

The marked event at UTC 05:51:07.000 could be a short spike with a maximum count of 4294 photons [50]. Short spikes, that could be GRBs, have a typical duration of 50 ms to 100 ms and the rate of short spikes observed in the ACS count rate is about 30 spikes per day [35].

The same procedure can be made for the rebinned data to an 8 second time binning of November 29, 2004 UTC 08:02:20.800 in figure 5.16a.

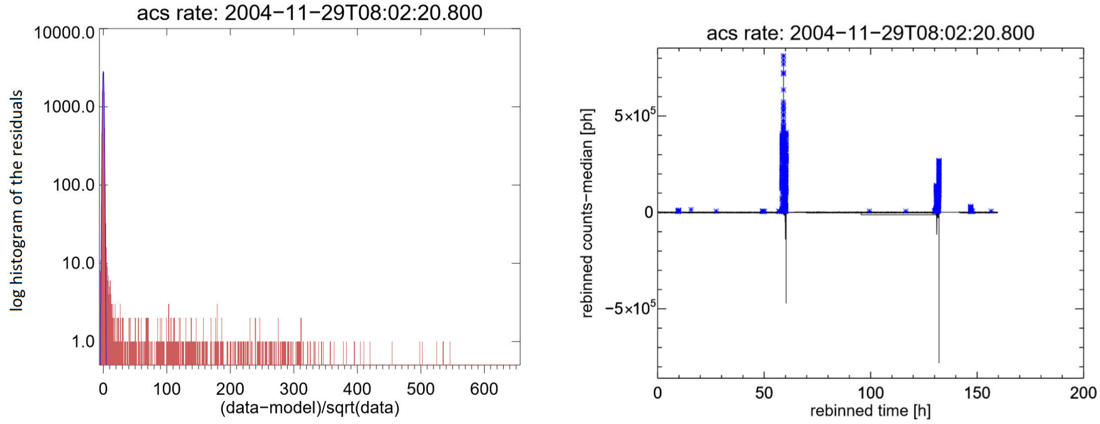

(a) The logarithmic histogram of the residuals with a superimposed Gaussian function.

(b) The rebinned count rate to an 8 second time binning.

Figure 5.21: The count rate of the ACS on November 29, 2004 UTC 08:02:20.800. The data are rebinned to an 8 second time binning and a median filter of length 300 time bins is used. The left figure shows the logarithmic histogram of the residuals and a Gaussian function. The right figure shows significant counts, marked in blue.

Many residuals above 5σ are wrongly measured as 'signals', but they originate from the strong increase of the photon flux when INTEGRAL enters the radiation belts.

Finally, the logarithmic histogram density of the residuals of January 1, 2006 UTC 00:00:00.000 (figure 5.16b) can be shown in figure 5.22.

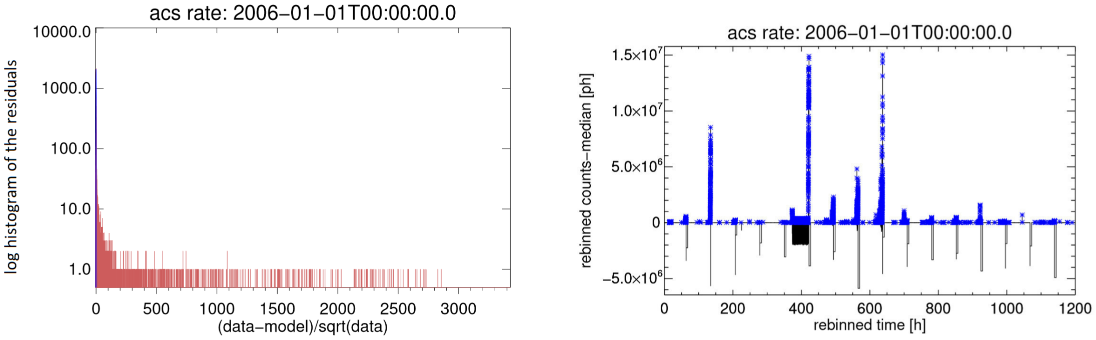

(a) The logarithmic histogram of the residuals with a superimposed Gaussian function.

(b) The rebinned count rate to a one minute time binning.

Figure 5.22: The count rate detected by the ACS on January 1, 2006 UTC 00:00:00.000. The data are rebinned to a one minute time binning and a median filter of length 300 time bins is used. The left figure shows the logarithmic histogram of the residuals and a Gaussian function. The right figure shows significant counts, marked in blue.

5.2.2 Example for an observed gamma-ray burst with data from the Anticoincidence Shield

The ACS can be used as GRB monitor that has been explained before in section 4.2.2. The described procedure in section 5.2.1 for finding events with a significance higher than 5σ can be applied on the following example to calculate the distance of an object.

The received data from the ACS on January 1, 2016 UTC 00:00:00.000 are shown in figure 5.23.

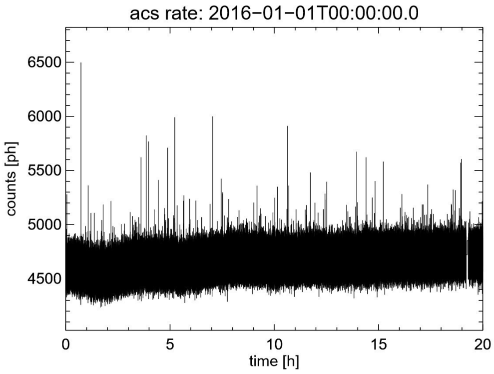

Figure 5.23: The count rate detected by the ACS on January 1, 2016 UTC 00:00:00.000 with a bin size of one second.

The next step is the counting of events that fall into an interval of bin size 0.125. This is demonstrated in a histogram in figure 5.24a. Finally, possible events outside the Gaussian curve are marked in blue in figure 5.24b.

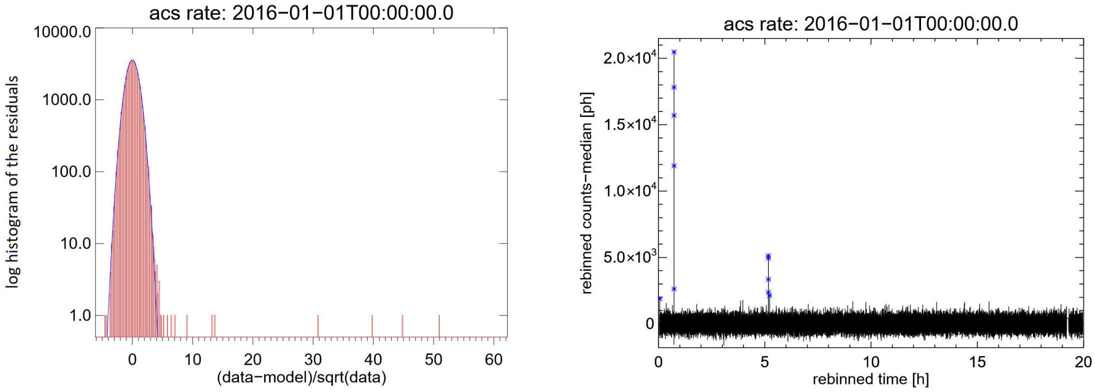

(a) The logarithmic histogram of the residuals with a superimposed Gaussian function.

(b) The rebinned count rate to a one second time binning minus the background.

Figure 5.24: The measured ACS count rate on January 1, 2016 UTC 00:00:00.000. The left figure shows the logarithmic histogram of the residuals with a superimposed Gaussian function in blue and the right figure presents possible events with a significance larger than 5σ.

Two distinct peaks can be observed in figure 5.24b. By looking at these peaks more precisely, light curves can be produced. These are shown in figure 5.25 and present the evolution of the released photons of the GRBs [50].

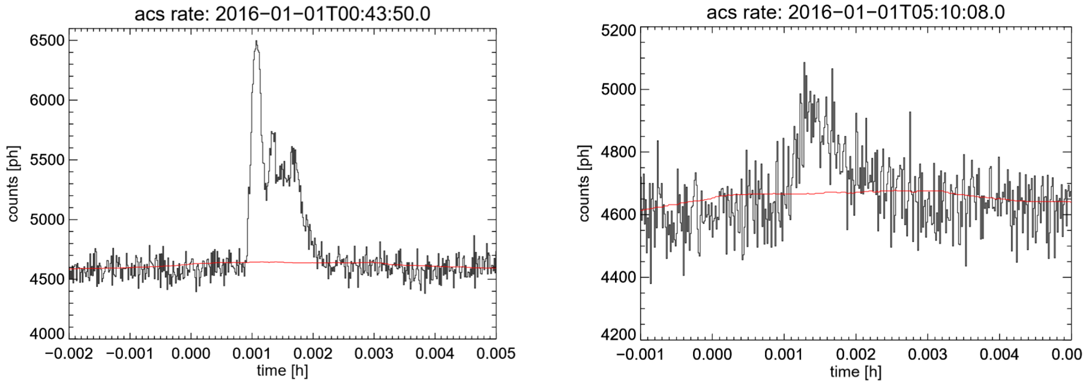

(a) The light curve of GRB 160101A around 00:43:53.271 UTC with a duration of 5 s and a maximum count of 6498 photons.

(b) The light curve of GRB 160101B around 05:10:11.825 UTC with a duration of 6 s and a maximum count of 5086 photons.

Figure 5.25: Light curves of two GRBs, GRB 160101A with a duration of 5 s and GRB 160101B with a duration of 6 s. Shown in red is a median filter of length 300 time bins as a background model.

The distance d between the ACS and a GRB can be calculated from equation 5.6.

$$L = 4\pi d^2 F \tag{5.6}$$

The parameter L gives the luminosity which is the total amount of energy E that is radiated from an object per second (L = E/s) and F is the photon flux that is the number of photons received from an object per unit area and per second (F = # photons/cm^{2}s) [51]. The luminosity of short GRBs is in the range 10^{51} erg/s - 10^{53} erg/s, where the mean (10^{52} erg/s) is used for the calculation of the GRB's distances [52]. The effective area is $5000 cm^2$ on average, the duration of the burst is 5 s and 6 s, respectively and the total counts are 61014 photons and 8512 photons [35]. This results in a photon flux of F = 2.4 ph/cm^{2}s for GRB 160101A and a photon flux of F = 0.3 ph/cm^{2}s for GRB 160101B. The photon flux can be calculated in units of erg/cm^{2}s. For this, the energy of one photon can be estimated as 300 keV [53]. Since 1 keV = 1.602 $\cdot 10^{-19}$ J and 1 J = 10^7 erg, the energy of one photon in units of erg is: 1 ph = 300 keV = 3 $\cdot 10^5 \cdot$ 1.602 $\cdot 10^{-19} \cdot 10^7$ erg = 4.8 $\cdot 10^{-7}$ erg. The photon flux of GRB 160101A then is F = 2.4 $\cdot \frac{4.8 \cdot 10^{-7} erg}{cm^2 s}$ = 1.2 $\cdot 10^{-6} \frac{erg}{cm^2 s}$ and the photon flux of GRB 160101B is F = 0.3 $\cdot \frac{4.8 \cdot 10^{-7} erg}{cm^2 s}$ = 1.4 $\cdot 10^{-7} \frac{erg}{cm^2 s}$.

The distance d between GRB 160101A and the ACS can now be calculated, using equation 5.6:

$$d = \sqrt{\frac{L}{4\pi F}} = \sqrt{\frac{10^{52} \cdot erg \cdot cm^2 s}{4\pi \cdot 1.2 \cdot 10^{-6} \frac{erg}{cm^2 \cdot s}}} = 3 \cdot 10^{28} cm = 10 Gpc, \tag{5.7}$$

The unit 1 pc is equal to 3 $\cdot 10^{18}$ cm.
Similarly, the distance d between GRB 160101B and the ACS can be estimated:

$$d = \sqrt{\frac{L}{4\pi F}} = \sqrt{\frac{10^{52} \cdot erg \cdot cm^2 s}{4\pi \cdot 1.4 \cdot 10^{-7} \frac{erg}{cm^2 \cdot s}}} = 7.5 \cdot 10^{28} cm = 25 Gpc \tag{5.8}$$

These results must be treated carefully, because the assumed luminosity and energy of one photon are average values.

5.2.3 Bayesian blocks for model independent analysis

Another method for the analysis of intensity variations in a given count rate is with Bayesian statistics. For this method, the data set is described as a continuous spectrum of counting data that extends over a broad range of timescales, which is called the global process, and signals that are not part of the global process. These signals are local and can be random or periodic. Now, the aim is to distinguish between global and local signals and to find a change point that is the point where the intensity of the count rate changes. At the end, the count rate is segmented in intervals of time where the signal may safely be taken as constant; in this way, the segmentation tells us about the time variability of the signal that is recognised as being clearly significant and supported by the measurement itself. The illustration of the intervals is called Bayesian blocks (figure 5.26).

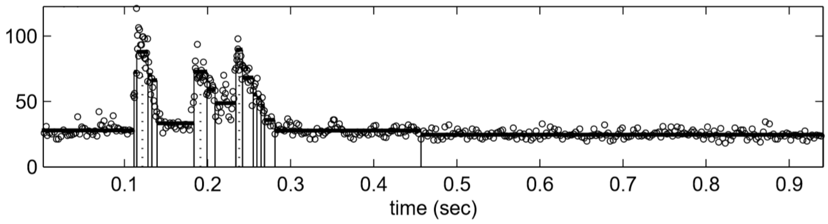

Figure 5.26: Bayesian blocks for a binned count rate. The different intensities are segmented in several subintervals that are defined through the maximum probability for a point being the change point. From [54].

One form of the Bayes's Theorem for estimating parameters is given in equation 5.9. Some data D are given and a model M with a parameter Θ.

$$P(\Theta|D,M)P(D|M) = P(D|\Theta,M)P(\Theta|M) \tag{5.9}$$

The factor $P(\Theta|D,M)$ is the posterior probability density of the parameter Θ, given the data and the model, and $P(D|M)$ is the prior probability for the data, given the model, which is sometimes called the global likelihood. The likelihood of the parameter is given in $P(D|\Theta,M)$ and the prior probability of the parameter, given the model, is $P(\Theta|M)$. Based on the data D and any prior information, it is now the aim to find out the probability for the correctness of the model, and to find likely values for the parameters.

As explained above, the outputs are the most probable intervals for constant intensities. However, it is possible that for a given data set the probability for a model without change point is larger than that with change point. For this, two models can be compared. The first model M_1 has a constant intensity of counts N over an observation time interval T and is also called the unsegmented model. The second model M_2 is a segmented model and has two different constant intensities in two subintervals $T_1 + T_2 = T$.

The global likelihood of each model, which is also the evidence for the model, in a set of K models, can be calculated with the following equation.

$$L(M_k, D) = \int P(D|\Theta_k, M_k)P(\Theta_k|M_k)d\Theta_k = \frac{\Gamma(N+1)}{(M+1)^{N+1}} \tag{5.10}$$

Because equation 5.10 only depends on the count rate N and the intervals M, the global likelihood for an unsegmented model for binned data is $L(M_1|D) = \Phi_D(N,M)$ and for a segmented model with a change point, the global likelihood for binned data is given through $L(M_2|D) = \Phi(N_1,M_1)\Phi(N_2,M_2)$. In case of the segmented model, the probability for every single point being the change point is calculated and the maximum probability at the end is the point where a significant variation in the intensity is given [54].

Figure 5.27 shows an example for estimating the likelihood for a change point (equation 5.10) for data with photon arrival times T = [1,2,3,4,5,6,7,8,9,10] in seconds and counts N = [1,1,1,1,1,10,10,10,10,10].

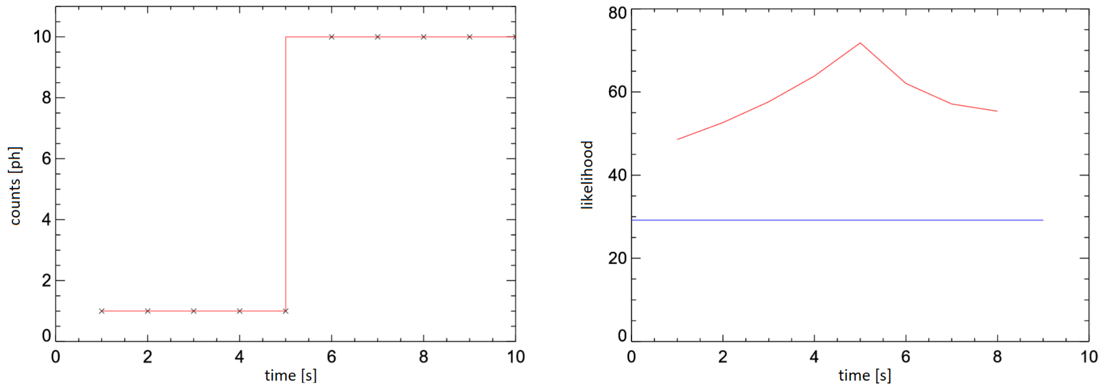

(a) The change point segments the count rate in two intervals of time with constant intensities.

(b) The likelihood for the change point in a segmented (red) and unsegmented (blue) model.

Figure 5.27: The likelihood for the change point in a segmented (red) and unsegmented (blue) model (right). The change point segments the count rate in two intervals of time (left), where the intensities may be taken as constant.

The likelihood is the highest for the arrival time 5 s, which is then set as the change point. At this time, the intensity changes from 1 count to 10 counts and is constant in the segmented intervals. The algorithm explained here can also be applied on the ACS count rate for extracting localized signals from the count rate data [54].

6 Applying the methods

The above described methods for characterizing data from the ACS and subtracting the background from these data (section 5) can now be applied and used for measuring the signal-to-noise ratio (SNR) of the ACS. Several histograms that were created for bin sizes of 50 ms, one second, 8 seconds and one minute can be added up for each year to obtain a histogram of the over-all residuals. The resulting histogram is then superimposed with a Gaussian function and a power law (i.e. straight line in a log-log representation). The power law is presented by a tail of the distribution, which is the part that represents significant but rare events. A variable x obeys a power law if it follows a probability distribution

$$f(x) = B \cdot \left(\frac{x}{10}\right)^{\alpha} \cdot e^{-\beta/x} \tag{6.1}$$

Here, B is the amplitude of the power law, α represents the slope of the distribution function, which is normalised to 10, and β describes the exponential cutoff.

The following histograms are superimposed with a power law, as explained above, a Gaussian function (section 5.1) and a total fit function of both, which has the following form:

$$f(x) = A \cdot e^{-\frac{(x-x_0)^2}{2\sigma^2}} + B \cdot \left(\frac{x}{10}\right)^{\alpha} \cdot e^{-\beta/x} = N + S \tag{6.2}$$

The first term describes the noise and the second term the signal. Thus, the SNR R = S/N can be calculated, which is the ratio of the areas of the two functions limited to the x-axis of values larger than 3σ. The area is estimated by integrating the PDF over a certain interval, which, in this case, is from 3σ to infinity. The value 3σ comes from the three-sigma rule, explained in section 5.1, which means that there is a possibility of 99.73 % for a measured count being a signal. We compare the part of the data of the power law function to the tail of the Gaussian fluctuations around the 'uninteresting' ('background'), i.e. we compare the tail of the Gaussian beyond 3 width units of the Gaussian away from its mean. The uncertainty of the SNR σ_R can be measured through the propagation of uncertainty with the following formula, where $\sigma_S = \sqrt{S}$ and $\sigma_N = \sqrt{N}$:

$$\sigma_R = \sqrt{\left(\frac{\partial R}{\partial S}\right)^2 \sigma_S^2 + \left(\frac{\partial R}{\partial N}\right)^2 \sigma_N^2} = \frac{S}{N}\sqrt{\frac{1}{S} + \frac{1}{N}} = R\sqrt{\frac{1}{\sigma_S^2} + \frac{1}{\sigma_N^2}} \tag{6.3}$$

Figure 6.1a and b show the logarithmic histogram of the over-all residuals of bin size 50 ms for the year 2007 with a number of 120 histograms and for the year 2008 with a number of 513 histograms that are summed up. The blue curve shows the Gaussian function, the green curve shows the power law and the red curve is the total fit function.

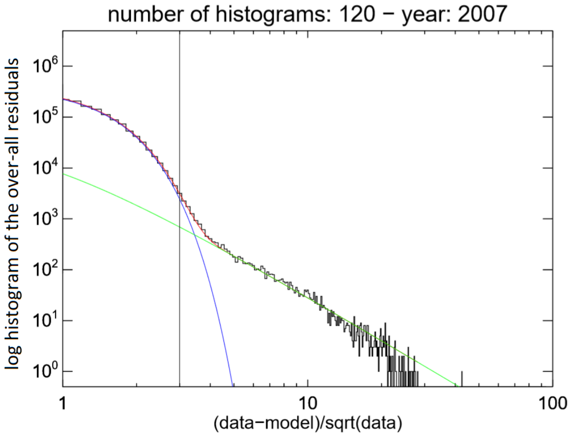

(a) bin size 50 ms.

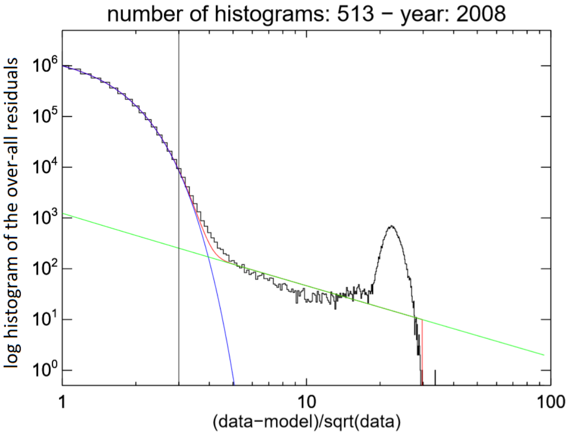

(b) bin size 50 ms.

Figure 6.1: The logarithmic histogram of the over-all residuals of 120 and 513 data sets of the ACS count rate with a bin size of 50 ms and a median filter of 300 for the years 2007 and 2008. The Gaussian function is shown in blue, the power law in green and the total fit is shown in red. The large number of residuals at around 20σ (right) comes from an increase in the count rate at the beginning of the annealing period January 12, 2008 to January 31, 2008. The SNR for 2007 is $\text{SNR} = 1.542 \pm 0.068$ and for 2008 the $\text{SNR} = 0.502 \pm 0.015$.

The fit parameter in figure 6.1a are as follows: $x_0 = -0.1111 \pm 0.0035$, $\sigma = 0.9665 \pm 0.0013$ and $\alpha = -2.885 \pm 0.022$ and the parameters in figure 6.1b are: $x_0 = -0.0697 \pm 0.0018$, $\sigma = 0.9330 \pm 0.0006$ and $\alpha = -1.403 \pm 0.023$. The resulting SNRs for the years 2007 and 2008 are 1.542 ± 0.068 and 0.502 ± 0.015.

The next figures (figures 6.2a and b) show examples for the logarithmic histogram of the over-all residuals of the rebinned count rate to a one second time binning and a median filter of length 300 time bins for the years 2005 and 2008.

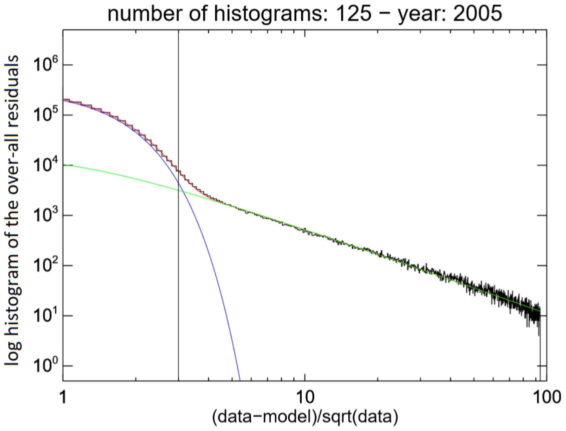

(a) bin size one second.

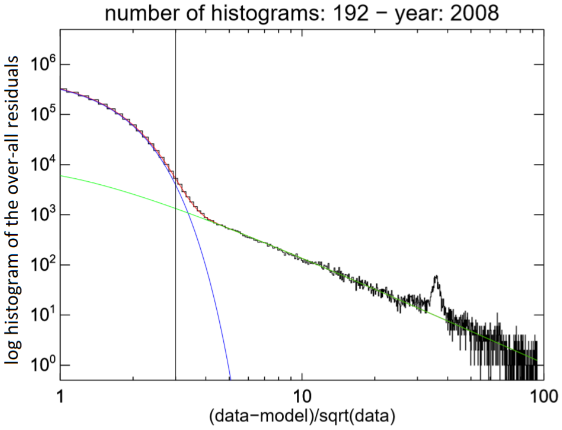

(b) bin size one second.

Figure 6.2: The logarithmic histogram of the over-all residuals of 125 and 192 data sets of the ACS count rate with a bin size of one second and a median filter of 300 for the years 2005 and 2008. The Gaussian function is shown in blue, the power law in green and the total fit is shown in red. Again, the large number of residuals at around 30-40σ (right) comes from an increase in the count rate at the beginning of the annealing period January 12, 2008 to January 31, 2008. The SNR for 2005 is SNR $= 8.577 \pm 0.217$ and for 2008 the SNR $= 3.072 \pm 0.095$.

The parameter of the total fit are $x_0 = -0.2072 \pm 0.0042$, $\sigma = 1.0788 \pm 0.0017$ and $\alpha = -1.709 \pm 0.005$ for 2005 and $x_0 = -0.1160 \pm 0.0027$, $\sigma = 0.9820 \pm 0.0011$ and $\alpha = -2.145 \pm 0.011$ for the year 2008. The corresponding SNRs are 8.577 ± 0.217 for 2005 and 3.072 ± 0.095 for 2008.

For a rebinning of the ACS count rate to an 8 second time binning, the logarithmic histogram of the over-all residuals has, for example, the following forms (figure 6.3a and b).

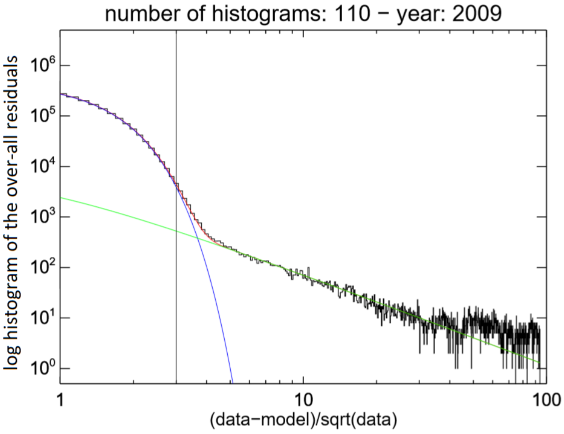

(a) bin size 8 seconds.

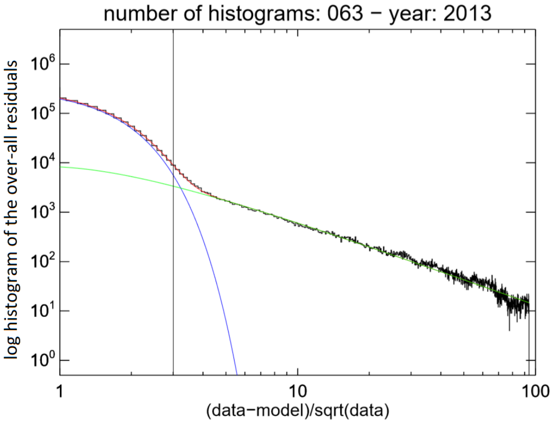

(b) bin size 8 seconds.

Figure 6.3: The logarithmic histogram of the over-all residuals of 110 and 63 data sets of the ACS count rate with a bin size of 8 seconds and a median filter of 300 for the years 2009 and 2013. The Gaussian function is shown in blue, the power law in green and the total fit is shown in red. The SNR for 2009 is SNR $= 1.606 \pm 0.0.040$ and for 2013 the SNR $= 7.442 \pm 0.134$.

The fit parameter in figure 6.3a are as follows: $x_0 = -0.1047 \pm 0.0019$, $\sigma = 0.9967 \pm 0.0007$ and $\alpha = -1.733 \pm 0.010$ and the parameters in figure 6.3b are: $x_0 = -0.1879 \pm 0.0037$, $\sigma = 1.1092 \pm 0.0015$ and $\alpha = -1.706 \pm 0.005$. The resulting SNRs for the years 2009 and 2013 are $1.606 \pm 0.0.040$ and 7.442 ± 0.134.

Finally, the Gaussian fit and the power law fit can be drawn in the logarithmic histogram of the over-all residuals (figure 6.4a and b) that where calculated by rebinning the data to a one minute time binning and a median filter of length 300 time bins.

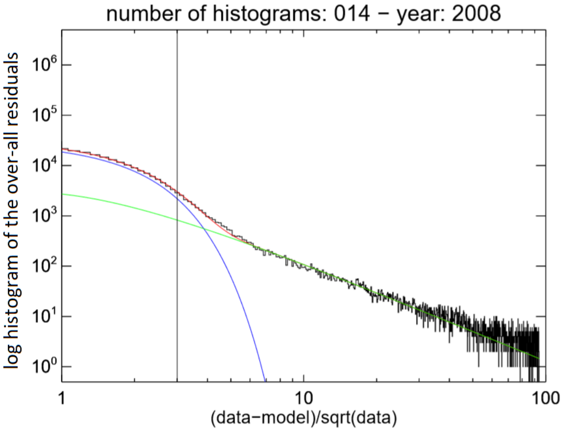

(a) bin size one minute.

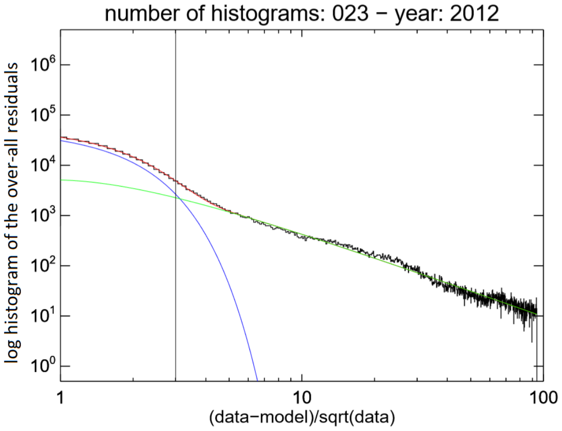

(b) bin size one minute.

Figure 6.4: The logarithmic histogram of the over-all residuals of 14 and 23 data sets of the ACS count rate with a bin size of one minute and a median filter of 300 for the years 2008 and 2012. The Gaussian function is shown in blue, the power law in green and the total fit is shown in red. The SNR for 2008 is SNR $= 2.138 \pm 0.067$ and for 2012 the SNR $= 7.556 \pm 0.201$.

The parameter of the total fit are $x_0 = -0.9943 \pm 0.0331$, $\sigma = 1.6721 \pm 0.0115$ and $\alpha = -1.978 \pm 0.013$ for 2008 and $x_0 = -0.8920 \pm 0.0286$, $\sigma = 1.5331 \pm 0.0100$ and $\alpha = -1.699 \pm 0.006$ for the year 2012. The corresponding SNRs are 2.138 ± 0.067 for 2008 and 7.556 ± 0.201 for 2012.

The above given examples of the logarithmic histograms of the over-all residuals (figures 6.1, 6.2, 6.3 and 6.4) show different values of the standard deviation σ and the mean value x_0 of the Gaussian distribution function, different values of the slope α of the power law distribution and thus varying values of the SNR. These parameters can now be compared to each other within the years 2003 and 2017.

The distribution of the parameter x_0 over the years 2003 to 2017 can be seen in figure 6.5. This parameter represents the mean of the Gaussian function that is explained in section 5.1.

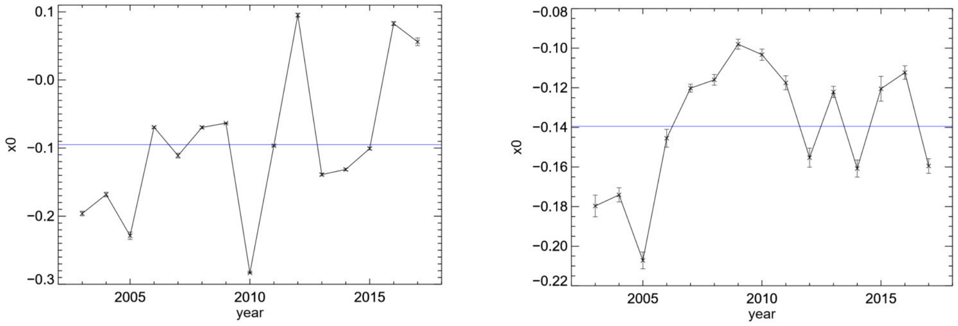

(a) bin size 50 ms.

(b) bin size one second.

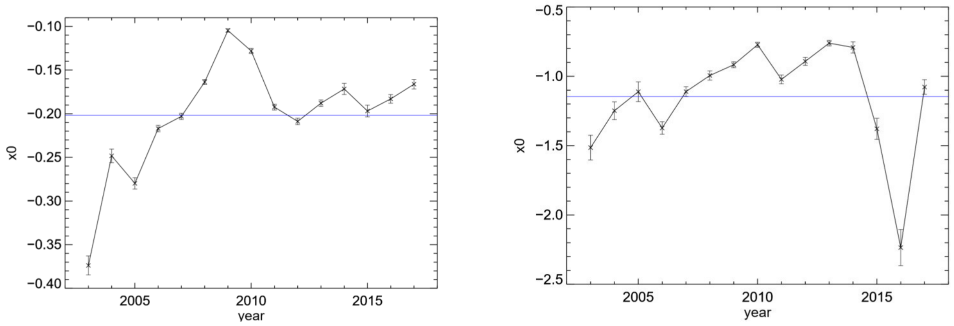

(c) bin size 8 seconds.

(d) bin size one minute.

Figure 6.5: Distribution of the parameter x_0 of the Gaussian function within the years 2003 and 2017 with bin sizes of 50 ms (upper left), 1 s (upper right), 8 s (lower left) and 60 s (lower right). The horizontal line shows the mean value of all x_0 values.

The values of x_0 are in the range of -0.28 and 0.10 for data in 50 ms time bins (figure 6.5a), and in the range of -0.21 and -0.10 for rebinned data in a one second time binning (figure 6.5b). For a binning to an 8 second time binning (figure 6.5c) the x_0 values are between -0.37 and -0.10 and finally, the x_0 values are between -2.24 and -0.77 for rebinned data in a one minute time binning (figure 6.5d). The blue horizontal lines represent the mean values of x_0. All values (with exception of the values binned to a one minute time binning) are relatively stable around the mean of all x_0 values, which means that they are more or less constant. One exception is given for the rebinned data to a one minute time binning, where the x_0 values are at least constant. This means that the offset increases with an increasing time binning. The mean value x_0 of the Gaussian distribution function fluctuates between positive an negative values, but mainly the centroid has negative values. This shift to negative values is a systematical effect. For a better plotting of the Gaussian function and for calculating the mean x_0, only positive values of the logarithmic histogram were used, so the fit is not subject to fluctuations between positive and negative values. Consequently, the IDL curvefit function does not know the distribution of the negative values, so the plot can not be done correctly and is shifted to negative values in order to still make a good fit. The tendency for the evolution of the mean value x_0 for the years over the mission time is to higher values, i.e. to zero. Since most of the mean values are negative, they are outside the fit area and these peak values are estimated by how good the histogram agrees with a Gaussian curve.

Additionally, as a consequence of the shift of the mean x_0 to negative values, the 3 σ threshold is not the same as if x_0 would be 0 in the standard normal distribution. This means that the noise is moved to negative values by x_0 what, on the other hand, influences the SNR.

The next parameter that is discussed over the years 2003 to 2017 for different time binnings (figure 6.6) is the standard deviation σ of the mean value x_0 of the Gaussian distribution function that measures the fluctuations of the data around the expected value.

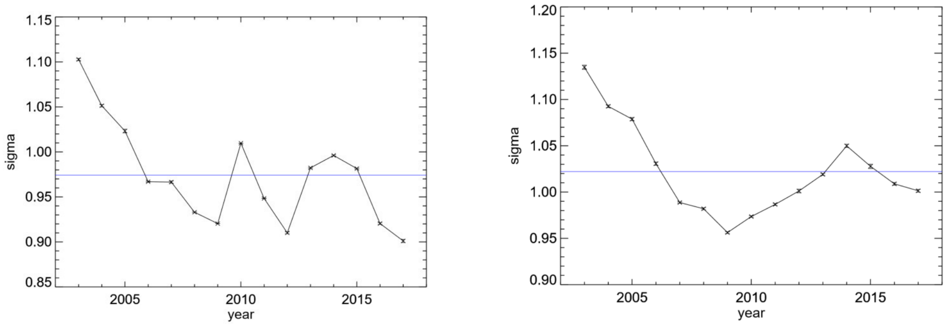

(a) bin size 50 ms. (b) bin size one second.

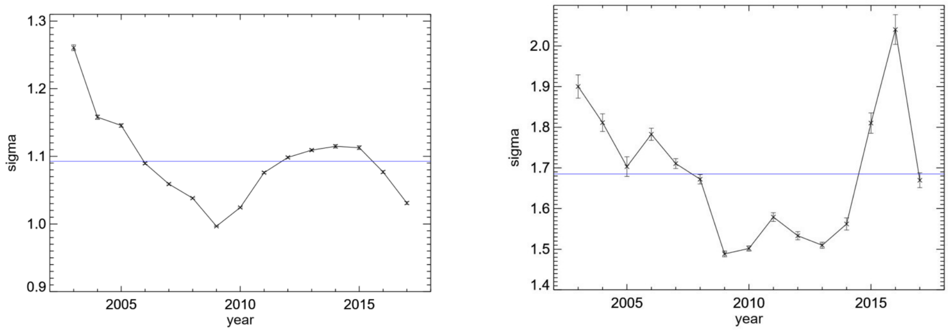

(c) bin size 8 seconds. (d) bin size one minute.

Figure 6.6: Distribution of the parameter σ of the Gaussian function within the years 2003 and 2017 with bin sizes of 50 ms (upper left), 1 s (upper right), 8 s (lower left) and 60 s (lower right). The horizontal line shows the mean value of all σ values.

The data of the logarithmic histogram of the over-all residuals of the analyzed ACS count rate per 50 ms time bins, present values of σ between 0.90 and 1.10 (figure 6.6a). For the data binned to a one second time binning, σ ranges from 0.96 to 1.13 (figure 6.6b). Figure 6.6c shows values of σ from 1.00 to 1.26 for a binned count rate to an 8 second time binning and figure 6.6d lastly presents σ values between 1.49 and 2.04 for bin sizes of one minute. Over the mission, the standard deviation σ changes its value and decreases. The evolution of this parameter can be observed as being inversely to the eleven-year solar cycle (figure 5.2). In the year 2009, when the Sun reaches its minimum of solar activity, the parameter σ has its smallest value (except for count rate data per 50 ms time bins, but also here, σ is very small). The initial assumption for a correction factor of 1.2 to the data's statistical error is not correct. It is only right for specific data sets and totally wrong for rebinned data to a one minute time binning (figure 6.6d). In general, the standard deviation σ decreases over time, which leads to the assumption that the ACS looses its sensitivity. The measured count rate tends to be close to the expected value, which is the mean x_0, because of the decreasing standard deviation σ.

The two parameters x_0 and σ of the Gaussian distribution function can be related with each other, which is shown in figure 6.7.

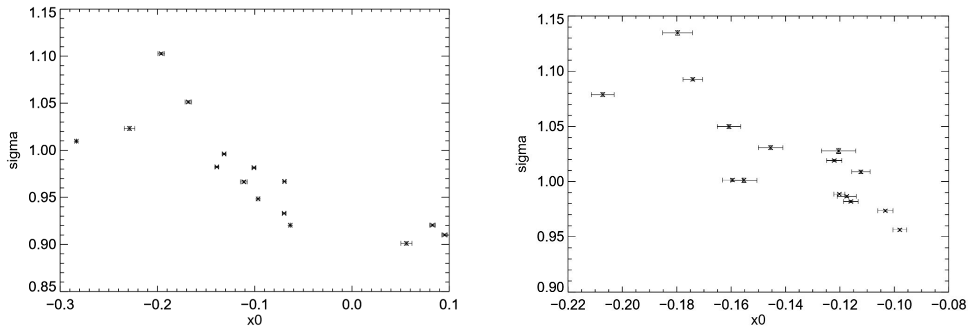

(a) bin size 50 ms.

(b) bin size 1 s.

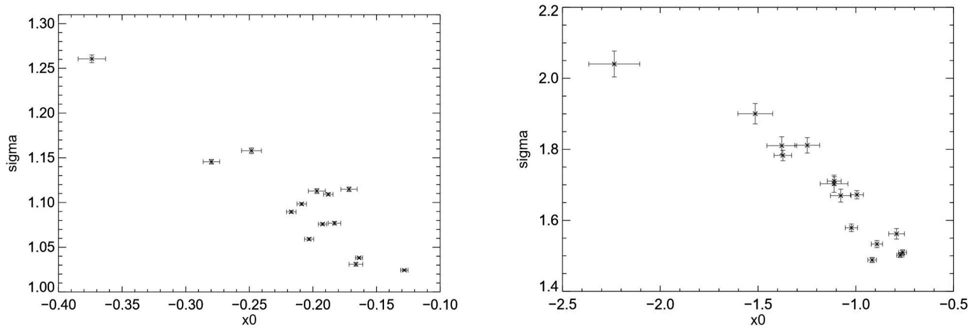

(c) bin size 8 s.

(d) bin size 60 s.

Figure 6.7: The evolution of the parameters x_0 and σ of the Gaussian function distribution within the years 2003 and 2017 with bin sizes of 50 ms (upper left), 1 s (upper right), 8 s (lower left) and 60 s (lower right).

For smaller values of x_0, the fluctuations around the mean become larger, because the negative x_0 values try to offset the large σ values. This means that x_0 and σ are anti-correlated and it can be observed in all four cases of different bin sizes. The standard normal distribution is defined as the distribution with a mean value $x_0 = 0$ and variance $\sigma^2 = 1$, as explained in section 5.1. The larger the deviation of σ from $\sigma = 1$, the more is the mean value x_0 shifted to negative values and the larger is the systematical uncertainty of the centroid of the Gaussian function.

The evolution from 2003 to 2017 of the parameter α of the power law distribution, described above, can be seen in the next figure 6.8.

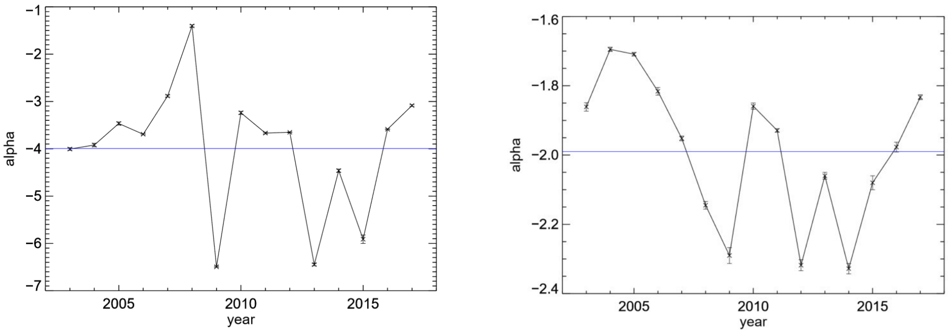

(a) bin size 50 ms.

(b) bin size one second.

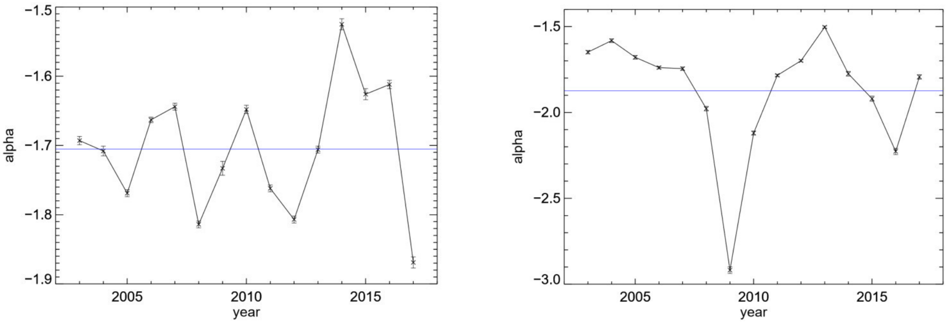

(c) bin size 8 seconds.

(d) bin size one minute.

Figure 6.8: Distribution of the parameter α of the power-law within the years 2003 and 2017 with bin sizes of 50 ms (upper left), 1 s (upper right), 8 s (lower left) and 60 s (lower right). The horizontal line shows the mean value of all α values.

The minimum value of α for the analyzed data per 50 ms time bins is -6.50, and the maximum value is -1.40 (figure 6.8a). In figure 6.8b, α values between -2.33 and -1.70 can be observed for the years 2003 to 2017 for data binned to a one second time binning. For data binned to an 8 second time binning, α is in the range of -1.87 and -1.53 (figure 6.8c). Finally, figure 6.8d presents values of α between -1.50 and -2.92 for data binned to a one minute time binning. The parameter α of the power law distribution, described above, gives the slope of the distribution function that is always negative. The uncertainty of each value is small, which means that the varying α values are not statistics. They fluctuate around the mean value of all α values (see blue horizontal line) with only one exception in 2009 for data binned to a one minute time binning in figure 6.8d. The slope of the power law distribution in 2009 is in three of four cases for a different time binning (expect 6.8c) very small. This means that the slope is steeper, so consequently less significant events were observed in the added up histograms of the over-all residuals of this year for each time binning. During the active phase of the Sun in 2009, the number of solar flares is small, which could lead to a small number of significant events.

In addition, a possible correlation between the slope α and the number of summed up histograms of the over-all residuals N can be discussed. The following figure 6.9 shows the number of histograms N plotted against the slope α.

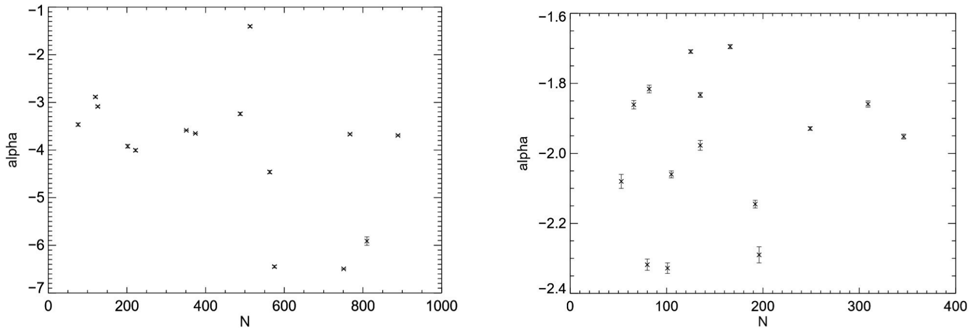

(a) bin size 50 ms.

(b) bin size one second.

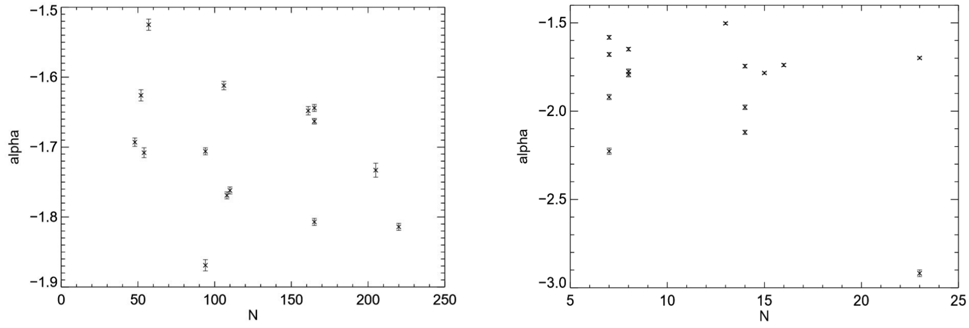

(c) bin size 8 seconds.

(d) bin size one minute.

Figure 6.9: The number of histogram densities N of the residuals of analyzed data per 50 ms time bins (upper left), binned to a one second (upper right), 8 second (lower left) and one minute (lower right) time binning plotted against the value α of the power law distribution function within the years 2003 to 2017.

The four figures in 6.9 do not present a correlation between the plotted parameter N and α. This means that the slope of the power law distribution is independent of the number of histograms of the over-all residuals.

At least, the signal-to-noise ratios of the ACS can be determined for different time binnings. This is presented in figure 6.10.

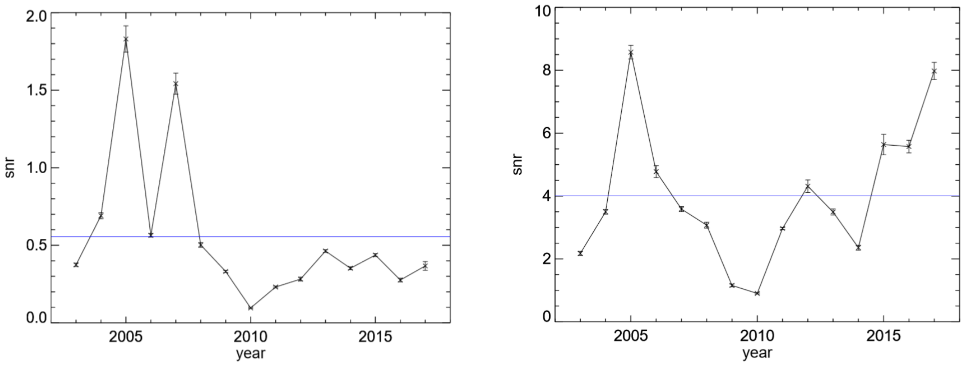

(a) bin size 50 ms.

(b) bin size one second.

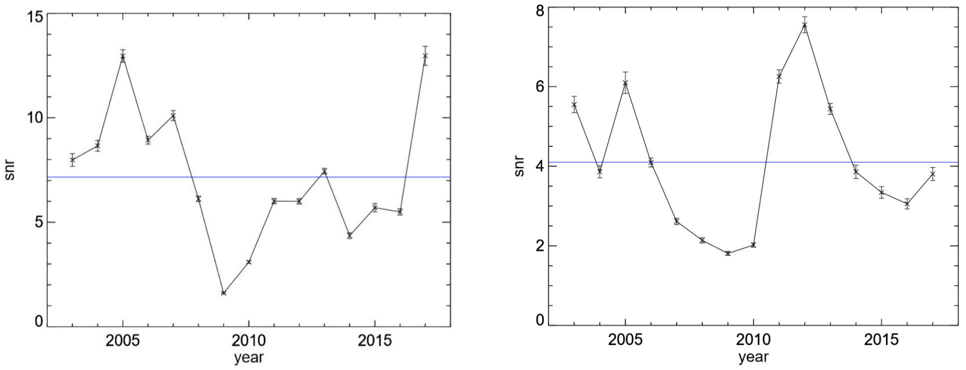

(c) bin size 8 seconds.

(d) bin size one minute.

Figure 6.10: Distribution of the SNR values within the years 2003 and 2017 with bin sizes of 50 ms (upper left), 1 s (upper right), 8 s (lower left) and 60 s (lower right). The horizontal line shows the mean value of all SNR values.

The SNR in figure 6.10a ranges between 0.23 and 1.83 for data per 50 ms time bins. For data binned to a one second time binning, the SNR has values of 0.90 to 8.58 (figure 6.10b) and for data binned to an 8 second time binning, the values are between 1.61 and 12.97 (figure 6.10c). The SNR in figure 6.10d has values of 1.81 and 7.56 for binned data to a one minute time binning.

The SNR decreases from 2003 to 2009 and then increases again. The evolution of this parameter can be seen as a large sinus curve. The small values of the SNR in 2009 are related to the solar minimum in this year. The weak magnetic field of the Sun, as explained in section 5.1, can not shield the Earth from cosmic rays, which leads to an increase of the count rate of the ACS. The high count rate, however, makes the detection of possible events more difficult, so that the signal-to-noise ratio becomes smaller. Another influence on the SNR are the entries of INTEGRAL in the Van Allen radiation belts and also the shift of the mean value x_0 to negative values, as explained above.

The SNR's statistical errors are actually higher than calculated with equation 6.3. The propagation of uncertainty for functions of the form $R = \frac{S}{N}$ provides an additional term of $-2\frac{\sigma_{SN}}{SN}$ under the square-root. Since the parameter S and N are anti-correlated, their uncertainty σ_{SN} is negative, which leads to a higher uncertainty on the SNR. This additional parameter is not included in the propagation of uncertainty, because the parameter σ_{SN} could not be calculated in this way of fit procedure.

7 Conclusion

The INTEGRAL spacecraft is in space for more than 15 years now. This provides a huge amount of data from all of its instruments. In this thesis, the measured count rate of the ACS for about 14 years (2003 to 2017) has been analyzed. With its large effective are, the SPI veto system can detect photons above 75 keV from all directions in the Universe. The count rate varies between 80000 counts/s and 160000 counts/s and it is the goal to understand the origin of these variations. The count rate can be split into an 'interesting' part that varies on shorter timescales and that originates from transients such as GRBs, solar flares or novae and into an 'uninteresting' part that varies on shorter timescales and comes from orbital cosmic ray exposure variations. The latter is the background and in this thesis, the median filter was discussed as a background model. It was subtracted from the data for obtaining the significant part, the signals.

These signals and the background can be related to each other to find out how much significant information can be found in the data. The value of the signal-to-noise ratio changes over the years. The reason for this is the variations in the count rate that can either come from outside the spacecraft or from inside. The Sun has a great impact on the measured count rate. During its eleven-year cycle, the detection of gamma-rays from celestial sources has different difficulty levels. When the Sun is at its most active phase, several solar flares can be detected and the magnetic field of the Sun is strong enough to shield the Earth from cosmic rays. This leads to a decrease in the ACS background rate, whereas the count rate increases during the minimum of solar activity, when the Sun's magnetic field is weak. In this time, it is more difficult to measure signals from celestial sources, because of the high background rate. This effect can be observed in the small values of the signal-to-noise ratio in 2009 and 2010, when the Sun's weak magnetic field can not shield the Earth from cosmic radiation.

On the other hand, the ACS count rate changes over the mission because of impacts from inside the instrument. The BGO crystals are damaged by cosmic ray interactions and consequently, the counting method in the BGO crystals changes. This can be seen in the parameter σ of the Gaussian distribution function that describes the fluctuations around the expected mean of the count rate. The standard deviation σ decreases with time. As a consequence, because of a smaller width of the distribution function, and also because of the shift of x_0 to negative values, counts that would have been detected as noise before can now be detected as signal. This means that signals must be treated and interpreted differently depending on the detection time of the signal. The varying mean x_0 and standard deviation σ leads to the result that the initial assumption of a Poisson distributed count rate with a correction factor 1.2 is not correct. The fluctuations around the varying mean value means that the distribution is similar to a Poisson distribution, but not exactly the same.

All these effects must be known when searching for significant events in the ACS count rate data.

Bibliography

[1] *Processes that Create Cosmic Gamma Rays*, `https://imagine.gsfc.nasa.gov/science/toolbox/gamma_generation.html`, Accessed: 06.04.2018, 2010.

[2] C. Winkler, T. J.-L. Courvoisier, G. Di Cocco, N. Gehrels, A. Giménez, S. Grebenev, W. Hermsen, J. M. Mas-Hesse, F. Lebrun, N. Lund, G. G. C. Palumbo, J. Paul, J.-P. Roques, H. Schnopper, V. Schönfelder, R. Sunyaev, B. Teegarden, P. Ubertini, G. Vedrenne, and A. J. Dean, »The INTEGRAL mission«,, vol. 411, pp. L1–L6, Nov. 2003. DOI: `10.1051/0004-6361:20031288`.

[3] *Radioactivity and Radioisotopes*, `https://www.nde-ed.org/Education\Resources/HighSchool/Radiography/radioactivity.htm`, Accessed: 11.03.2018.

[4] *Guide to the Nuclear Wallchart*, `http://www2.lbl.gov/abc/wallchart/\outline.html`, Accessed: 11.03.2018, 2000.

[5] *Die Kernphysik*, `http://www.hpwt.de/Kern2.htm`, Accessed: 20.03.2018.

[6] M. Hernanz, »Novae in γ-rays«, *Bulletin of the Astronomical Society of India*, vol. 40, p. 377, Sep. 2012. arXiv: `1301.1660 [astro-ph.HE]`.

[7] *Principles of positron annihilation*, `https://sundoc.bibliothek.uni-halle.de/diss-online/08/08H048/t2.pdf`, Accessed: 12.03.2018.

[8] ——, »Gamma-ray Emission from Nova Outbursts«, in *Stellar Novae: Past and Future Decades*, P. A. Woudt and V. A. R. M. Ribeiro, Eds., ser. Astronomical Society of the Pacific Conference Series, vol. 490, Dec. 2014, p. 319. arXiv: `1305.0769 [astro-ph.HE]`.

[9] Z. Kuncic, *PHYS 5012 - Radiation Physics and Dosimetry*, `http://www.physics.usyd.edu.au/~kuncic/lectures/RP3_slides.pdf`, Accessed: 11.03.2018, 2013.

[10] *Planck's Constant Definition*, `https://www.thoughtco.com/definition-of-plancks-constant-605523`, Accessed: 02.04.2018.

[11] *Wie schnell ist Lichtgeschwindigkeit?*, `https://www.lichtmikroskop.net/optik/lichtgeschwindigkeit.php`, Accessed: 02.04.2018.

[12] A. Zimmerman Jones, *The Photoelectric Effect*, `https://www.thoughtco.com/the-photoelectric-effect-2699352`, Accessed: 08.03.2018, 2017.

[13] C. R. Nave, *Compton Scattering*, http://hyperphysics.phy-astr.gsu.edu/hbase/quantum/comptint.html, Accessed: 10.03.2018, 2017.

[14] M. Sampoorna, *Compton Scattering in Astrophysics*, http://www.iucaa.in/~dipankar/ph217/contrib/compton.pdf, Accessed: 10.03.2018, 2003.

[15] *Pair Production and Annihilation*, http://electrons.wikidot.com/pair-production-and-annihilation, Accessed: 18.03.2018.

[16] C. Crawford, *The Transient Universe – Transcript*, https://www.gresham.ac.uk/lectures-and-events/the-transient-universe, Accessed: 15.03.2018, 2014.

[17] R. Diehl, D. H. Hartmann, and N. Prantzos, Eds., *Astronomy with Radioactivities*, vol. 812, Lecture Notes in Physics, Berlin Springer Verlag, 2011. DOI: 10.1007/978-3-642-12698-7.

[18] N. Straumann, »The Role of the Exclusion Principle for Atoms to Stars: A Historical Account«, *eprint arXiv:quant-ph/0403199*, Mar. 2004. eprint: quant-ph/0403199.

[19] *CNO cycle*, http://astronomy.swin.edu.au/cosmos/C/CNO+cycle, Accessed: 08.04.2018.

[20] *How Big is the Sun? | Size of the Sun*, https://www.space.com/17001-how-big-is-the-sun-size-of-the-sun.html, Accessed: 02.04.2018.

[21] *The Diversity of the Sun*, http://www.leibniz-kis.de/en/research/the-sun/, Accessed: 23.03.2018.

[22] J. Kiener, M. Gros, V. Tatischeff, and G. Weidenspointner, »Properties of the energetic particle distributions during the October 28, 2003 solar flare from INTEGRAL/SPI observations«,, vol. 445, pp. 725–733, Jan. 2006. DOI: 10.1051/0004-6361:20053665. eprint: astro-ph/0511091.

[23] K. Nomoto, N. Tominaga, M. Tanaka, K. Maeda, and H. Umeda, »Nucleosynthesis in Core-Collapse Supernovae and GRB-Metal-Poor Star Connection«, in *Supernova 1987A: 20 Years After: Supernovae and Gamma-Ray Bursters*, S. Immler, K. Weiler, and R. McCray, Eds., ser. American Institute of Physics Conference Series, vol. 937, Oct. 2007, pp. 412–426. DOI: 10.1063/1.3682938. arXiv: 0707.2187.

[24] *Doomed Neutron Stars Create Blast of Light and Gravitational Waves*, https://svs.gsfc.nasa.gov/12740, Accessed: 18.03.2018, 2017.

[25] E. Nakar, »Short-hard gamma-ray bursts«, vol. 442, pp. 166–236, Apr. 2007. DOI: 10.1016/j.physrep.2007.02.005. eprint: astro-ph/0701748.

[26] R. Diehl, »Nuclear astrophysics lessons from INTEGRAL«, *Reports on Progress in Physics*, vol. 76, no. 2, p. 026 301, 2013. [Online]. Available: http://stacks.iop.org/0034-4885/76/i=2/a=026301.

[27] *"Rosetta stone" found to decode the mystery of gamma ray bursts*, https://www.nasa.gov/centers/goddard/news/topstory/2003/0618rosettaburst.html, Accessed: 18.03.2018, 2013.

[28] R. S. Mallozzi, *The Transient Universe – Transcript*, `https://gammaray.nsstc.nasa.gov/batse/grb/duration/`, Accessed: 17.03.2018, 2014.

[29] R. Diehl, T. Siegert, J. Greiner, M. Krause, K. Kretschmer, M. Lang, M. Pleintinger, A. W. Strong, C. Weinberger, and X. Zhang, »INTEGRAL/SPI γ-ray line spectroscopy«, *ArXiv e-prints*, Oct. 2017. arXiv: `1710.10139 [astro-ph.IM]`.

[30] H. Zell, *Radiation Belts – Fun Facts*, `https://www.nasa.gov/mission_pages/rbsp/mission/fun-facts.html`, Accessed: 21.02.2018, 2017.

[31] A. von Kienlin, N. Arend, G. G. Lichti, A. W. Strong, and P. Connell, »Gamma-ray burst detection with INTEGRAL/SPI«, in *X-Ray and Gamma-Ray Telescopes and Instruments for Astronomy.*, J. E. Truemper and H. D. Tananbaum, Eds., ser., vol. 4851, Mar. 2003, pp. 1336–1346. DOI: `10.1117/12.461141`. eprint: `astro-ph/0302139`.

[32] G. Vedrenne, J.-P. Roques, V. Schönfelder, P. Mandrou, G. G. Lichti, A. von Kienlin, B. Cordier, S. Schanne, J. Knödlseder, G. Skinner, P. Jean, F. Sanchez, P. Caraveo, B. Teegarden, P. von Ballmoos, L. Bouchet, P. Paul, J. Matteson, S. Boggs, C. Wunderer, P. Leleux, G. Weidenspointner, P. Durouchoux, R. Diehl, A. Strong, M. Cassé, M. A. Clair, and Y. André, »SPI: The spectrometer aboard INTEGRAL«,, vol. 411, pp. L63–L70, Nov. 2003. DOI: `10.1051/0004-6361:20031482`.

[33] *INTEGRAL Science Data Centre SPI Analysis User Manual*, `http://www.isdc.unige.ch/integral/download/osa/doc/10.2/osa_um_spi.pdf`, Accessed: 23.03.2018, 2015.

[34] *INTEGRAL pictures and videos*, `http://integral.esa.int/integ_pictures.html`, Accessed: 19.03.2018.

[35] V. Savchenko, A. Neronov, and T. J.-L. Courvoisier, »Timing properties of gamma-ray bursts detected by SPI-ACS detector onboard INTEGRAL«,, vol. 541, A122, A122, May 2012. DOI: `10.1051/0004-6361/201218877`. arXiv: `1203.1344 [astro-ph.HE]`.

[36] *The Electromagnetic Spectrum*, `https://science.nasa.gov/ems/12_gammarays`, Accessed: 21.02.2018.

[37] Saint-Gobain Ceramics & Plastics, Inc., *BGO Bismuth Germanate*, `https://www.crystals.saint-gobain.com/products/bgo`, Accessed: 21.02.2018, 2016.

[38] R. Engstrom, *Photomultiplier Handbook*, `http://psec.uchicago.edu/links/Photomultiplier_Handbook.pdf`, Accessed: 21.02.2018, 1980.

[39] a. U.-P. D. I. K. Lichtscheidl, *Aufbau eines CLSM*, `https://www.univie.ac.at/mikroskopie/3_fluoreszenz/clsm/2f_pmt.htm`, Accessed: 21.02.2018.

[40] SENSE, *Photomultiplier Tubes (PMT)*, `https://www.sense-pro.org/lll-sensors/pmt`, Accessed: 22.02.2018.

[41] C. Guidorzi, *The 3rd Interplanetary Network*, `http://www.fe.infn.it/~guidorzi/doktorthese/node23.html`, Accessed: 19.02.2018, 2003.

[42] *INTEGRAL Picture Of the Month (POM) Archive [2001-2018]*, https://www.cosmos.esa.int/web/integral/pom-archive, Accessed: 31.03.2018.

[43] M. I. Ribeiro, *Gaussian Probability Density Functions: Properties and Error Characterization*, http://users.isr.ist.utl.pt/~mir/pub/probability.pdf, Accessed: 26.03.2018.

[44] *Distributions of One Variable*, http://work.thaslwanter.at/Stats/html/\statsDistributions.html, Accessed: 30.03.2018, 2015.

[45] *Three-sigma rule*, https://www.encyclopediaofmath.org/index.php/Three-sigma_rule, Accessed: 26.03.2018, 2011.

[46] T. Yaqoob, *How Many Sigma?*, http://exoplanetsdigest.com/2012/02/\06/how-many-sigma/, Accessed: 30.03.2018, 2012.

[47] T. Hebbeker, *Statistik - Fehlerrechnung - Auswertung von Messungen*, https://web.physik.rwth-aachen.de/~hebbeker/lectures/stat_fprakt_1.pdf, Accessed: 30.03.2018.

[48] K. Grace-Martin, *Differences Between the Normal and Poisson Distributions*, https://www.theanalysisfactor.com/differences-between-normal-and-poisson-distributions/, Accessed: 30.03.2018.

[49] *What Is Robustness in Statistics?*, https://www.thoughtco.com/what-is-robustness-in-statistics-3126323, Accessed: 07.04.2018.

[50] *INTEGRAL Gamma-Ray Bursts*, http://isdc.unige.ch/integral/science/\grb, Accessed: 30.03.2018.

[51] *Luminosity and Apparent Brightness*, https://www.e-education.psu.edu/astro801/content/l4_p4.html, Accessed: 31.03.2018.

[52] J. M. Burgess, »A Bayesian Analysis of the Golenetskii Relation«, in *Eighth Huntsville Gamma-Ray Burst Symposium*, ser. LPI Contributions, vol. 1962, Oct. 2016, p. 4033.

[53] J. M. Burgess, J. Greiner, D. Bégué, and F. Berlato, »A Bayesian Fermi-GBM Short GRB Spectral Catalog«, *ArXiv e-prints*, Oct. 2017. arXiv: 1710.08362 [astro-ph.HE].

[54] J. D. Scargle, »Studies in Astronomical Time Series Analysis. V. Bayesian Blocks, a New Method to Analyze Structure in Photon Counting Data«,, vol. 504, pp. 405–418, Sep. 1998. DOI: 10.1086/306064. eprint: astro-ph/9711233.

List of Figures

List of Tables

Appendix

Additional tables.

year	N	α	σ	x_0	signal/noise
2003	222	-4.006 ± 0.028	1.1027 ± 0.0012	-0.1961 ± 0.0034	0.374 ± 0.011
2004	202	-3.921 ± 0.037	1.0513 ± 0.0013	-0.1682 ± 0.0033	0.691 ± 0.020
2005	76	-3.466 ± 0.033	1.0232 ± 0.0021	-0.2287 ± 0.0054	1.830 ± 0.085
2006	889	-3.693 ± 0.013	0.9669 ± 0.0005	-0.0694 ± 0.0013	0.564 ± 0.011
2007	120	-2.885 ± 0.022	0.9665 ± 0.0013	-0.1111 ± 0.0035	1.542 ± 0.068
2008	513	-1.403 ± 0.023	0.9330 ± 0.0006	-0.0697 ± 0.0018	0.502 ± 0.015
2009	751	-6.495 ± 0.012	0.9204 ± 0.0001	-0.0634 ± 0.0002	0.331 ± 0.007
2010	488	-3.240 ± 0.031	1.0097 ± 8.8412e-05	-0.2833 ± 0.0002	0.096 ± 0.004
2011	767	-3.668 ± 0.018	0.9484 ± 0.0003	-0.0965 ± 0.0009	0.231 ± 0.006
2012	374	-3.652 ± 0.009	0.9101 ± 0.0010	0.0952 ± 0.0028	0.282 ± 0.012
2013	575	-6.448 ± 0.025	0.9823 ± 0.0006	-0.1389 ± 0.0019	0.463 ± 0.009
2014	563	-4.462 ± 0.033	0.9961 ± 0.0007	-0.1314 ± 0.0018	0.352 ± 0.010
2015	810	-5.912 ± 0.089	0.9815 ± 0.0006	-0.1007 ± 0.0020	0.437 ± 0.009
2016	351	-3.587 ± 0.009	0.9205 ± 0.0010	0.0828 ± 0.0029	0.276 ± 0.012
2017	126	-3.086 ± 0.020	0.9011 ± 0.0018	0.0560 ± 0.0057	0.367 ± 0.028

Table 1: The columns describe (from left to right) the year, for which the data are received, the parameter α of the power law distribution function, the standard deviation σ and the mean value x_0 of the Gaussian distribution function and the signal-to-noise ratio. The data used for the calculation of α, σ, x_0 and signal/noise are per 50 ms time bins.

year	N	α	σ	x_0	signal/noise
2003	66	-1.861 ± 0.012	1.1348 ± 0.0023	-0.1797 ± 0.0055	2.173 ± 0.066
2004	166	-1.695 ± 0.006	1.0926 ± 0.0014	-0.1741 ± 0.0036	3.496 ± 0.073
2005	125	-1.709 ± 0.005	1.0788 ± 0.0017	-0.2072 ± 0.0042	8.577 ± 0.217
2006	82	-1.816 ± 0.011	1.0307 ± 0.0018	-0.1455 ± 0.0045	4.775 ± 0.190
2007	346	-1.952 ± 0.007	0.9887 ± 0.0008	-0.1202 ± 0.0020	3.585 ± 0.078
2008	192	-2.145 ± 0.011	0.9820 ± 0.0011	-0.1160 ± 0.0027	3.072 ± 0.095
2009	196	-2.290 ± 0.023	0.9563 ± 0.0010	-0.0980 ± 0.0025	1.155 ± 0.046
2010	309	-1.859 ± 0.009	0.9736 ± 0.0009	-0.1033 ± 0.0028	0.901 ± 0.020
2011	249	-1.929 ± 0.005	0.9867 ± 0.0011	-0.1175 ± 0.0035	2.969 ± 0.034
2012	80	-2.318 ± 0.016	1.0012 ± 0.0020	-0.1553 ± 0.0048	4.313 ± 0.200
2013	105	-2.060 ± 0.010	1.0191 ± 0.0011	-0.1221 ± 0.0028	3.491 ± 0.097
2014	101	-2.328 ± 0.015	1.0499 ± 0.0018	-0.1608 ± 0.0043	2.356 ± 0.078
2015	53	-2.080 ± 0.020	1.0278 ± 0.0024	-0.1205 ± 0.0063	5.637 ± 0.324
2016	135	-1.977 ± 0.014	1.0089 ± 0.0015	-0.1123 ± 0.0034	5.574 ± 0.201
2017	135	-1.833 ± 0.007	1.0014 ± 0.0015	-0.1595 ± 0.0037	7.977 ± 0.273

Table 2: See table 1. The data used are binned to a one second time binning.

year	N	α	σ	x_0	signal/noise
2003	48	-1.693 ± 0.006	1.2606 ± 0.0043	-0.3738 ± 0.0108	7.980 ± 0.304
2004	54	-1.708 ± 0.007	1.1579 ± 0.0032	-0.2483 ± 0.0078	8.659 ± 0.260
2005	108	-1.769 ± 0.005	1.1456 ± 0.0026	-0.2798 ± 0.0065	12.957 ± 0.300
2006	165	-1.663 ± 0.004	1.0896 ± 0.0015	-0.2170 ± 0.0037	8.927 ± 0.189
2007	165	-1.644 ± 0.005	1.0591 ± 0.0015	-0.2030 ± 0.0036	10.104 ± 0.238
2008	220	-1.814 ± 0.005	1.0382 ± 0.0012	-0.1637 ± 0.0028	6.120 ± 0.134
2009	205	-1.733 ± 0.010	0.9967 ± 0.0007	-0.1047 ± 0.0019	1.606 ± 0.040
2010	161	-1.648 ± 0.006	1.0244 ± 0.0010	-0.1281 ± 0.0029	3.091 ± 0.059
2011	110	-1.762 ± 0.005	1.0759 ± 0.0014	-0.1924 ± 0.0033	6.009 ± 0.127
2012	165	-1.807 ± 0.005	1.0984 ± 0.0015	-0.2088 ± 0.0037	6.600 ± 0.132
2013	94	-1.706 ± 0.005	1.1092 ± 0.0015	-0.1879 ± 0.0037	7.442 ± 0.134
2014	57	-1.525 ± 0.008	1.1148 ± 0.0025	-0.1716 ± 0.0064	4.356 ± 0.140
2015	52	-1.626 ± 0.008	1.1128 ± 0.0027	-0.1969 ± 0.0067	5.698 ± 0.201
2016	106	-1.612 ± 0.006	1.0769 ± 0.0019	-0.1830 ± 0.0049	5.494 ± 0.155
2017	94	-1.869 ± 0.008	1.0310 ± 0.0021	-0.1662 ± 0.0054	12.967 ± 0.454

Table 3: See table 1. The data used are binned to an 8 second time binning.

year	N	α	σ	x_0	signal/noise
2003	8	-1.649 ± 0.010	1.9003 ± 0.0287	-1.5143 ± 0.0891	5.552 ± 0.205
2004	7	-1.582 ± 0.011	1.8114 ± 0.0217	-1.2483 ± 0.0637	3.861 ± 0.153
2005	7	-1.679 ± 0.011	1.7031 ± 0.0242	-1.1112 ± 0.0708	6.099 ± 0.269
2006	16	-1.739 ± 0.008	1.7828 ± 0.0148	-1.3731 ± 0.0450	4.095 ± 0.114
2007	14	-1.745 ± 0.010	1.7106 ± 0.0121	-1.1103 ± 0.0355	2.613 ± 0.079
2008	14	-1.978 ± 0.013	1.6721 ± 0.0115	-0.9943 ± 0.0331	2.138 ± 0.067
2009	23	-2.918 ± 0.019	1.4883 ± 0.0072	-0.9166 ± 0.0218	1.809 ± 0.051
2010	14	-2.120 ± 0.012	1.5018 ± 0.0064	-0.7725 ± 0.0180	2.018 ± 0.054
2011	15	-1.784 ± 0.006	1.5790 ± 0.0107	-1.0224 ± 0.0312	6.256 ± 0.168
2012	23	-1.699 ± 0.006	1.5331 ± 0.0100	-0.8920 ± 0.0286	7.556 ± 0.201
2013	13	-1.503 ± 0.006	1.5097 ± 0.0074	-0.7608 ± 0.0202	5.441 ± 0.138
2014	8	-1.775 ± 0.014	1.5620 ± 0.0149	-0.7917 ± 0.0403	3.859 ± 0.168
2015	7	-1.920 ± 0.015	1.8103 ± 0.0250	-1.3788 ± 0.0761	3.342 ± 0.146
2016	7	-2.227 ± 0.018	2.0403 ± 0.0365	-2.2352 ± 0.1303	3.055 ± 0.128
2017	8	-1.793 ± 0.013	1.6696 ± 0.0182	-1.0772 ± 0.0527	3.805 ± 0.163

Table 4: See table 1. The data used are binned to a one minute time binning.

Acknowledgements

Hiermit möchte ich mich zuallererst bei Prof. Dr. Roland Diehl bedanken, der es mir ermöglicht hat, meine Bachelorarbeit bei ihm schreiben zu dürfen und der mich ermutigt hat, bei Gruppenmeetings den aktuellen Stand meiner Arbeit zu präsentieren.

Außerdem möchte ich mich bei meinem Betreuer, Dr. Thomas Siegert, bedanken, der immer Zeit für mich hatte um mir meine Fragen zu beantworten und der mich von Anfang bis Ende durch die Datenanalyse der SPI/ACS Daten geführt hat. Die vielen ausführlichen Gespräche über Astrophysik und die mittaglichen Kaffeepausen in der Gruppe haben mir sehr viel Spaß gemacht.

Ein großer Dank geht auch an meine Eltern, Dorothea und Michael, die immer an mich glauben und an meiner Arbeit interessiert sind und an meine Geschwister, Emilia und Fritz, die Tag und Nacht für mich da sind und mich jederzeit unterstützen.